

Nuclei of dwarf spheroidal galaxies KKs 3 and ESO 269-66 and their counterparts in our Galaxy

M. E. Sharina¹, V. V. Shimansky², and A. Y. Kniazev^{3,4,5,1}

¹*Special Astrophysical Observatory, Russian Academy of Sciences, N. Arkhyz, KCh R, 369167, Russia*

²*Kazan Federal University, Kremlevskaya 18, Kazan, 420008, Russia*

³*South African Astronomical Observatory, PO Box 9, 7935 Observatory, Cape Town, South Africa*

⁴*Southern African Large Telescope Foundation, PO Box 9, 7935 Observatory, Cape Town, South Africa*

⁵*Sternberg Astronomical Institute, Lomonosov Moscow State University, Moscow, Russia*

Accepted . Received ; in original form

ABSTRACT

We present the analysis of medium-resolution spectra obtained at the Southern African Large Telescope (SALT) for nuclear globular clusters (GCs) in two dwarf spheroidal galaxies (dSphs). The galaxies have similar star formation histories, but they are situated in completely different environments. ESO 269-66 is a close neighbour of the giant S0 NGC 5128. KKs 3 is one of the few truly isolated dSphs within 10 Mpc. We estimate the helium abundance $Y = 0.3$, age = 12.6 ± 1 Gyr, $[\text{Fe}/\text{H}] = -1.5, -1.55 \pm 0.2$ dex, and abundances of C, N, Mg, Ca, Ti, and Cr for the nuclei of ESO 269-66 and KKs 3. Our surface photometry results using HST images yield the half-light radius of the cluster in KKs 3, $r_h = 4.8 \pm 0.2$ pc. We demonstrate the similarities of medium-resolution spectra, ages, chemical compositions, and structure for GCs in ESO 269-66 and KKs 3 and for several massive Galactic GCs with $[\text{Fe}/\text{H}] \sim -1.6$ dex. All Galactic GCs possess Extended Blue Horizontal Branches and multiple stellar populations. Five of the selected Galactic objects are iron-complex GCs. Our results indicate that the sample GCs observed now in different environments had similar conditions of their formation ~ 1 Gyr after the Big Bang.

Key words: Dwarf galaxies: individual: KKs 3, ESO 269-66—globular clusters: individual: NGC 1904, NGC 5286, NGC 6254, NGC 6752, NGC 7089

1 INTRODUCTION

Many of the early-type dwarf galaxies contain old massive ($10^6 \div 10^7 M_\odot$) nuclei near their optical centres (Lotz et al. 2004, Sharina et al. 2005; Côté et al. 2006, Georgiev et al. 2009, Da Costa et al. 2009). These are located at the extreme high end of the GC mass function and constitute a large fraction of the total mass of these galaxies (Larsen et al. 2012). The mass of the nuclear star cluster correlates with the mass of the stellar spheroids of their host galaxies (Leigh et al. 2012). Characteristics of the nuclei provide important information about the physical conditions of the early host galaxy formation and evolution.

The existence of the phenomenon of multiple stellar populations in GCs is not completely understood (Charbonnel 2016 and references therein). One of the ideas is that these GCs are remnant nuclei of dwarf galaxies. In recent years, the number of observational facts related to this phenomenon has greatly increased (Gratton et al. 2012, Charbonnel 2016). High-resolution spectroscopic observations revealed correlated variations of C, N, O, Na, Al, Mg abun-

dances for stars in almost all old Galactic GCs (e.g. Carretta et al. 2010 and references therein). Chemical patterns of many Galactic GCs indicate that they contain several generations of stars and that the material from which GCs were formed was exposed to proton-capture processes at high temperatures. First stellar generations have chemical composition similar to that of the field stars. Second and subsequent (if any) stellar populations can be depleted in C and O, enhanced in N and Na. Helium enrichment in GCs appears to be correlated with the appearance of Extended Blue Horizontal Branches (EBHBs) and of Na–O and Al–Mg anti-correlations (D’Antona et al. 2002, Salaris et al. 2006, Chantereau et al. 2016). Hubble Space telescope (HST) observations in photometric filters sensitive to C, N, and O abundance variations allowed to disentangle splits of the main evolutionary sequences of Galactic and nearby extragalactic GCs (e.g. Piotto et al. 2015). A rare class of anomalous Galactic GCs was discovered (Table 10 in Marino et al. 2015 and references therein). These objects show variations in Fe and s-process element abundances. The most plausible

Table 1. Properties of dSphs KKs3 and ESO 269-66.

	KKs3	ESO 269-66
RA(J200.0)	2 ^h 24 ^m 44 ^s .4 ^a	13 ^h 13 ^m 09 ^s .1 ^b
Dec.(J200.0)	−73°30′51″ ^a	−44°53′24″ ^b
E(B − V)	0.045 ^a	0.093 ^b
Distance, Mpc	2.12 ^a	3.82 ^b
Diameter, kpc	1.5 ^a	2.4 ^b
V _T , mag	14.47 ^c	13.74 ^e
(V − I), mag	0.77 ^c	1.06 ^e
M _V	−12.3 ^c	−14.4 ^b
M _{HI} /L _B	0.03 ^c	< 0.002 ^b
M _{HI} , M _⊙	1.1 · 10 ⁵ ^c	< 0.9 · 10 ⁵ ^b
SFR _{12÷14Gyr} , M _⊙ yr ^{−1}	8.7 · 10 ^{−3} ^a	11 · 10 ^{−3} ^d
[Fe/H] _{12÷14Gyr} , dex	−1.9 ^a	−1.75 ^d

Notes: ^a: Karachentsev et al. (2015b), ^b: Karachentsev et al. (2013), ^c: Karachentsev, Kniazev & Sharina (2015a), ^d: Makarova et al. (2007), ^e Sharina et al. (2008).

explanation for the origin of these iron complex GCs is that they are remnant nuclei of dwarf galaxies (Bekki & Norris 2006).

Properties of our sample dSphs and their nuclei are summarized in Tables 1 and 2. ESO 269-66 is a dSph satellite of the peculiar giant elliptical Centaurus A=NGC 5128. The Cen A group with its numerous dwarf galaxies and tidal substructures is the only elliptical-dominated group within 10 Mpc (Karachentsev et al. 2007, Crnojević et al. 2016). The projected separation between NGC 5128 and ESO 269-66 is ∼198 kpc, which is typical of dSphs (Karachentsev et al. 2005, 2013). A considerable population of asymptotic giant branch (AGB) stars as a signature of the 2-3 Gyr old star formation was detected in ESO 269-66 (Crnojević et al. 2011). Stellar photometry using Hubble Space Telescope (HST) optical and infrared images indicates that at least three powerful star forming bursts happened in the galaxy 2±1.5, 3±1.5 (Crnojević et al. 2011), and 12-14 Gyr ago (Makarova et al. 2007). The last of the mentioned events was the most powerful. The mean metallicity of the oldest red giant branch (RGB) stars in ESO 269-66 is [Fe/H] ∼ −1.75 dex (Makarova et al. 2007). The stellar metallicity dispersion in ESO 269-66 is surprisingly large for a faint dSph (Karachentsev et al. 2007, Sharina et al. 2008). The dispersion of the stellar metallicities in ESO 269-66 is comparable to that of NGC 5237, a compact I0 type object with a central starburst, a suggested galaxy collision remnant (Thompson, 1992).

KKs3 is a unique highly isolated dSph recently discovered by Karachentsev et al. (2015b). It is one of the faintest known field galaxies (Karachentsev et al. 2015a). The arguments are: the colour-magnitude diagram (CMD) of the object consisting only of old (age > 1 Gyr) stars, the absolute magnitude M_V = −12.6 mag, effective surface brightness SB_{Ve} = 24.9 mag/arcsec^{−2}, neutral hydrogen mass-to-stellar mass ratio (M_{HI}/M^{*} = 10^{−2.34}) estimated by the luminosity of the galaxy in the K-band and star formation rate per unit galactic luminosity (specific star formation rate) sSFR = 10^{−13.6} estimated from the ultraviolet flux (Karachentsev et al. 2015a). For comparison, *sSFR* of a dwarf irregular galaxy having similar luminosity in the

Table 2. Properties of GCs in KKs3 and ESO 269-66.

	GC in KKs3	GC in ESO 269-66
(V − I) ₀ , mag	0.90±0.06 ^a	0.93 ^d
M _V , mag	−8.48 ^b	−9.9 ^d
R _h , pc	4.8 ± 0.2 ^a	2.5 ± 0.13 ^d
[Fe/H], dex	−1.55±0.2 ^a	−1.5±0.2 ^a
Age, Gyr	12.6±1.5 ^a	12.6±1.5 ^a
V _h , km s ^{−1}	316±7 ^c	774±6 ^a

^a: This work, ^b: Karachentsev et al. (2015b), ^c: Karachentsev et al. (2015a), ^d: Georgiev et al. (2009).

B-band is 2-2.5 orders of magnitude larger. The mass of the galaxy is 2 × 10⁷ M_⊙ (Karachentsev et al. 2015b). The nearest massive neighbour to KKs3 is M31 at a distance of ∼ 1.7 Mpc. A long-slit absorption-line spectrum of the GC in KKs3 which was taken with the RSS at the SALT in bright time in January 2015 allowed us to estimate radial velocity of the galaxy V_h = 316 ± 7 km s^{−1} (Karachentsev et al. 2015a). There was no neutral hydrogen detected in KKs3. The sSFR and M_{HI}/M^{*} parameters presented by Karachentsev et al. 2015a indicate that the galaxy has transformed most of its gas into stars.

Star formation histories of ESO 269-66 and KKs3 look similar. Three star forming bursts likely occurred in KKs3 12–14, 4–6, and 0.8–2 Gyrs ago (Karachentsev et al. 2015b), where the oldest one was the most powerful with mean [Fe/H] = −1.9 dex. Most stars (74%) of the galaxy were formed during this period (Karachentsev et al. 2015b).

We present the description of spectroscopic observations for the GCs in ESO 269-66 and KKs3 in Section 2. In Sections 3.1 and 3.2, we describe our methods developed for determination of ages, helium abundance (Y), [Fe/H] and the abundances of different chemical elements using medium-resolution optical spectra and present our results. We compare the spectra of the studied two nuclei with medium-resolution spectra of Galactic GCs from the library of Schiavon et al. (2005, hereafter Sch05)¹ and find possible Galactic analogues for our sample nuclei of dSphs (Sections 3.2.1, 3.2.2). We analyse CMDs of the selected Galactic GCs in Section 3.2.3. Structural and photometric parameters for the GC in KKs3 are presented in Section 4. Section 5 addresses the question: whether the GCs in KKs3 and ESO 269-66 host multiple stellar populations and what the origin of KKs3 and its nucleus is.

2 OBSERVATIONS AND DATA REDUCTION

The spectroscopic observations were carried out with SALT (Buckley et al. 2006, O’Donoghue et al. 2006) in the period of 15 January 2015 - 9 July 2015 (Table 3) with the Robert Stobie Spectrograph (RSS; Burgh et al. 2003, Kobulnicky et al. 2003). We used the long-slit mode with a slit width 1.25″, the grating pg0900, blocking filter pc03400 and the Camera

¹ The library by Sch05 contains high signal-to-noise integrated-light spectra of 40 Galactic GCs with *FWHM* ∼ 3.1 Å resolution including spectra of nine GCs with [Fe/H] ∼ −1.6 dex.

Table 3. Journal of spectroscopic observations.

Object	Date	T_{exp} (s)	Seeing (arcsec)
KKs 3	09/07/2015	3×900	1.6-1.8
	15-17/01/2015	5×1000	1-2
ESO 269-66	11/05/2015	3×900	~1
	1/06/2011	2×900	~1

Station parameter 26.5. The spectra cover a spectral range of 3700–6700 Å with a reciprocal dispersion of $0.97 \text{ Å pixel}^{-1}$ and spectral resolution of $\text{FWHM} = 5 \text{ Å}$. A 30-minute exposure in the same instrumental mode of the GC in ESO 269-66 was made during the commissioning time in July 2011. Primary reduction of the data was done with the SALT science pipeline (Crawford et al. 2010). The reduction of the SALT long-slit data was done in the way described by Kniazev et al. (2008). To improve the signal-to-noise ratio, the resulting one-dimensional spectra were smoothed using the adjacent-averaging method with five points window. The final signal-to-noise ratios in the resulting smoothed summary spectra of GCs in KKs 3 and ESO 269-66 reach ~ 100 at 5000 Å.

3 ANALYSIS OF THE SPECTRA

3.1 Method

The final medium-resolution spectra of the GCs in two dSphs are shown in Fig. 1 in comparison to the best-fitting model spectra computed as it is described below.

We used a program named *CLUSTER* (Sharina et al. 2013, 2014; Khamidullina et al. 2014) to calculate the synthetic integrated-light spectra for the GCs in ESO 269-66 and KKs 3. Appendix A in the paper by Sharina et al. (2014) explains the procedure and main principles of synthetic stellar spectra computation using models of stellar atmospheres. Synthetic spectra of stars were calculated according to their parameters: $[\text{Fe}/\text{H}]$, effective temperature, and surface gravity. These parameters were set by the scaled solar stellar evolutionary isochrones by Bertelli et al. (2008, hereafter B08), which include the horizontal branch (HB) and AGB stages and various helium content. These ingredients are necessary, in particular, to explain HB morphologies and splitting of evolutionary sequences of GCs in several distinct branches (B08 and references therein). We did not interpolate theoretical isochrones but used the available set. The calculated synthetic spectra of individual stars were summed according to the mass function by Chabrier (2005). The computation of the synthetic spectra takes into account about 600000 atomic and 1800000 ^{12}CH , ^{13}CH , and SiH molecular lines from the lists of Kurucz (1994) and Castelli & Kurucz (2003). The data for ten following molecules were kindly provided to us by Ya.V. Pavlenko: CN, VO, TiO, SO, SiO, NO, MgO, CO, and AlO. Calculations of the abundances of all elements except for H, Ca, and Mg were performed under the assumption of local thermodynamic equilibrium (LTE). Non-LTE effects were taken into account for H, Ca, and Mg as it was described by Sharina et al. (2013). The resulting model spectra of the GCs were normalized by the theoretical continuum and broadened to the resolution of

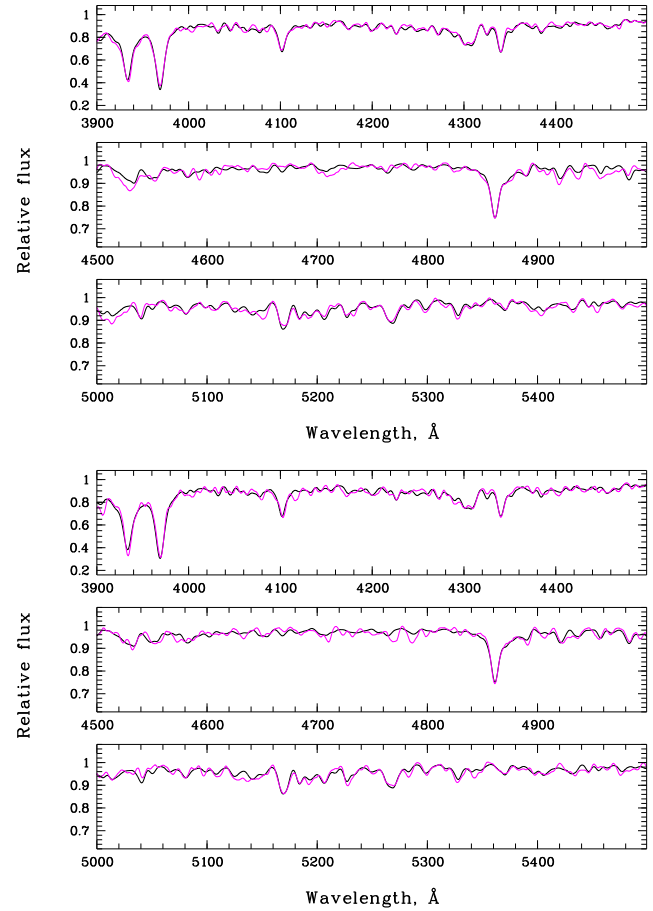


Figure 1. Continuum normalized rest-frame spectra of GCs in ESO 269-66 (top) and KKs 3 (bottom) in comparison to the model ones (black lines) calculated according to the elemental abundances described in Section 3 and Table 4.

the observed spectra. We determined chemical abundances by fitting the medium-resolution observed spectra with the computed models. To approximate the shape of the continuum in the observed spectra, we first smoothed the spectra by replacing each pixel value by the maximum of all points in the window $2 \cdot R + 1$, where $R = 10 \cdot \text{FWHM}$. Then we implemented the running mean with the radius of $10 \cdot \text{FWHM}$ to the filtered spectrum.

Ages and mean helium abundance (Y) for the GCs were determined by comparison of the observed and the model Balmer line profiles. The influence of these two parameters is not equivalent, which makes it possible to derive them simultaneously. The temperatures of the Main Sequence turn-off (MSTO) stars become higher with the decreasing age. This means that the depths of the cores and wings of the Balmer lines simultaneously strengthen. Increasing the Y values results in higher luminosities of hot HB stars. At the same time, temperatures and luminosities of stars populating Main Sequence (MS), sub-giant and red-giant branches do not change noticeably with the increasing of Y only and leaving all the other parameters unchanged (B08). Pressure broadening is not that significant in the atmospheres of HB stars, therefore, increasing of mainly Y results in strengthening of the central parts of Balmer lines in the integrated

spectra of GCs. The depths of H δ , H γ , and H β change differently with the change of Y, because hot HB stars contribute mainly to the blue part of the spectrum. The method is illustrated in Figs 2, A1 and A2 in Appendix A (please, see also Sharina et al. 2013, 2014; Khamidullina et al. 2014).

Almost all spectroscopic lines are blended at a resolution of FWHM ~ 5 Å. To derive chemical abundances we selected dominant features in the spectra mostly sensitive to the abundances of the specific spectroscopic elements. Iron gives a great number of spectral lines which allows its abundance to be derived with high accuracy. The depths of iron lines in the integrated synthetic and observed spectra of the GCs depend on [Fe/H] and micro-turbulent velocity (ξ_{turb}) (Figs B1, B2 in Appendix B). The last parameter in its turn depends on metallicities, log g, and T_{eff} of stars within the cluster (Malavolta et al. 2014 and references therein). The intensities of different iron lines are influenced by ξ_{turb} in a different rate (Figs B1, B2 in Appendix B). This fact allows us to select an optimum constant value of micro-turbulent velocity for calculation of synthetic spectra of GCs using stellar atmosphere models. The range of possible ξ_{turb} values for low-metallicity stars is $1.6 \div 2.2$ km s $^{-1}$ (e.g. Malavolta et al. 2014). To constrain [Fe/H] and ξ_{turb} at the resolution FWHM ~ 5 Å one can use, for example, such dominant blends as $\lambda \sim 5456, 5446, 5405, 5327, 5283, 5269, 5227, \text{ and } 5216$ Å with the shapes mostly changed by varying Fe and ξ_{turb} (please, see also a list of the most important atomic lines at the medium resolution in Fig. 2 by Dias et al. 2015). Given the similarity of the analysed spectra, we choose a constant ξ_{turb} value of 1.8 km s $^{-1}$ for all our sample GCs. When we used the relation from Marino et al. (2008), $\xi_{\text{turb}} = -0.254 \cdot \log g + 1.93$ (Malavolta et al. 2014), we obtained the following corrections to the elemental abundances in dex: $\Delta[\text{Fe}/\text{H}] = +0.08$, $\Delta[\text{C}/\text{Fe}] = -0.03$, $\Delta[\text{Mg}/\text{Fe}] = -0.04$, $\Delta[\text{Ca}/\text{Fe}] = -0.04$, $\Delta[\text{Ti}/\text{Fe}] = -0.04$, $\Delta[\text{Cr}/\text{Fe}] = -0.01$. It can be seen that these corrections are less than the errors of our analysis.

After fitting [Fe/H] and ξ_{turb} , we focused at the abundances of chemical elements which have prominent lines and blends in the spectroscopic range. Their depths may change by more than 1–3% of the continuum level while varying the corresponding abundances by 0.1–0.3 dex. These elements (and the corresponding spectroscopic features) are: calcium (CaII H+K; CaI $\lambda = 4226$ Å), magnesium (MgH molecule $\lambda \sim 4980 \div 5180$ Å, Mg I line 5183 Å), chromium (Cr lines $\lambda \sim 5207, 5298$ Å), nitrogen plus carbon (CN molecule $\lambda \sim 4120 \div 4220$ Å, carbon (CH 4300 Å band) (Figs B3 – B5 in Appendix B). The depth of the last spectroscopic feature decreases with an increase of oxygen abundance, but the amount of this change is ~ 5 times less than the line depth variation for carbon (e.g. Lardo et al. 2016). The abundance of oxygen was set $[\text{O}/\text{Fe}] \sim 0.5$ dex. According to our calculations, this value provides the correct shapes and depths of the CH-band 4300 Å and CN-band at $\lambda \sim 4120 \div 4220$ Å.

3.2 Results

The derived chemical abundances for two extragalactic and a comparative sample of five Galactic GCs are presented in Table 4. We used the spectra of Galactic GCs presented by Sch05. The isochrone providing the best fit of Balmer lines in

the spectra of all the sample GCs has the following parameters (B08): $Z = 0.0004$, $Y = 0.30$, and $\log(\text{Age}) = 10.10$. The abundance analysis of the Galactic GCs was performed using the same procedure as for two extragalactic GCs (Section 3.1). Errors of the elemental abundances (Table 4) include fitting uncertainties in an rms sense, signal-to noise effects, and the errors occurring due to the combined influence of several parameters on the spectrum such as micro-turbulent velocity, abundances of Fe, and several other elements. For instance, the strength of the CH-band at 4300 Å depends mainly on the C and O abundances. To a lesser extent, it depends also on ξ_{turb} and the abundances of Fe, Ti, Ca, Mg, Al, and Si.

We compared spectra of two nuclei not only with the computed theoretical ones but also with the medium-resolution spectra of Galactic GCs. It appears that spectra of five Galactic GCs from the library of Sch05 are very similar with the spectra of our two GCs in dSphs. These objects are NGC 5286, NGC 1904, NGC 6254, NGC 6752, and NGC 7089. Fig. 3 illustrates this comparison using the spectrum of NGC 5286 as an example. Comparison of the spectrum of NGC 5286 with the corresponding best-fitting synthetic one computed using the elemental abundances listed in Table 4 is shown in Fig. 4. Comparison of the NGC 5286 spectrum to the spectra of NGC 1904, NGC 5986, NGC 6254, NGC 6752, NGC 7089, and of several other Galactic GCs from the library by Sch05 having $[\text{Fe}/\text{H}] \sim -1.6$ dex is presented in Fig. A2 (Appendix A) and at an anonymous ftp site².

Appendix C demonstrates HST stellar photometric data for the GCs in ESO 269-66 and KKs3 and for the surrounding stellar fields. Probable contamination of intermediate-age high-metallicity stars to the integrated light of the GCs is considered. The presented analysis indicates that the contamination is small. Unfortunately, the central regions of the GCs are not resolved into individual stars due to crowding effects which are stronger for the more distant ESO 269-66. The probability to find bright projected foreground stars is higher for the GC in ESO 269-66, because the surface density and total number of intermediate-age high-metallicity stars is higher in this galaxy than that in KKs3.

Appendix D illustrates the similarity of absorption-line indices measured using flux-calibrated spectra in the Lick system (Burstein et al. 1984, Worthey et al. 1994, Worthey & Ottaviani 1997, Trager et al. 1998) for the sample extragalactic and Galactic GCs. The indices for the GCs in KKs3 and E269-66 calculated using the calibration of Katkov, Kniazhev & Sil'chenko (2015) are presented in Tables D1 and D2 together with the corresponding measurement errors. The total index errors consist of measurement errors and the errors of transformation to the Lick standard system. Lick indices for the Galactic GCs were taken from Schiavon et al. (2012). Fig. D1 shows two age-metallicity diagnostic plots of hydrogen-line indices H δ and H β versus the index $[\text{Mg}/\text{Fe}]'$ ³ and four diagnostic plots with indices that are sensitive to iron, Mg, Ca, C, N, and O. The α -enhanced models by Thomas et al. (2003, 2004) are over-plotted. Tables D1

² ftp://ftp.sao.ru/pub/sme/TwoDSphs/AppendixE.pdf

³ $[\text{Mg}/\text{Fe}]' = \sqrt{\text{Mgb}(0.72\text{Fe}5270 + 0.28\text{Fe}5335)}$

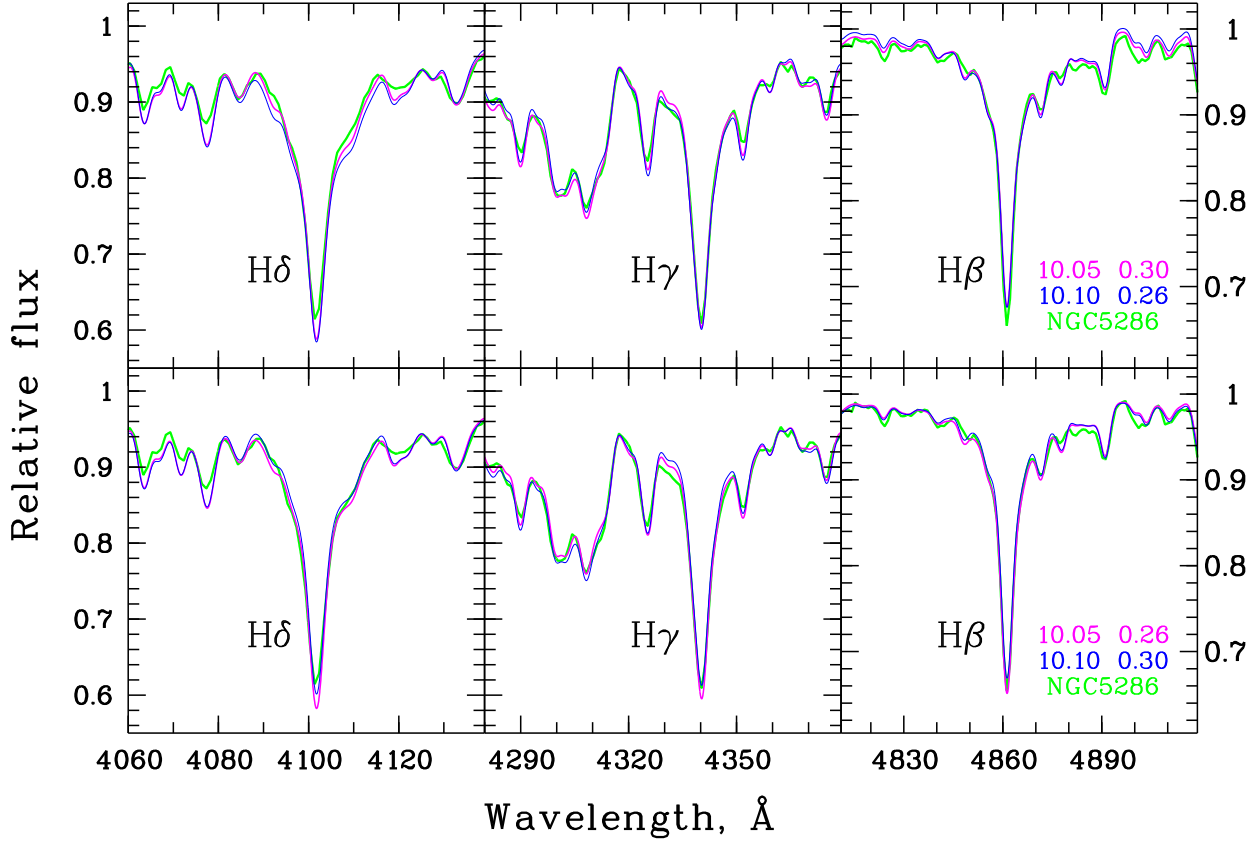


Figure 2. Comparison of three Balmer lines in the spectrum of NGC 5286 and computed synthetic integrated-light spectra. We used for the calculation the same elemental abundances valid for NGC 5286 (Table 4) and the isochrones by Bertelli et al. (2008) of the same metallicity $Z = 0.0004$ and different ages and specific helium abundances: $\log(\text{Age}) = 10.05, Y = 0.30$; $\log(\text{Age}) = 10.10, Y = 0.26$; $\log(\text{Age}) = 10.05, Y = 0.26$, and $\log(\text{Age}) = 10.10, Y = 0.30$. It can be seen that the last case provides a better agreement with the spectrum of NGC 5286

Table 4. Elemental abundances and their uncertainties for the GCs in KKs 3 and E269-66 and for five Galactic GCs according to our measurements using medium-resolution integrated-light spectra (Section 3).

GC	[Fe/H] (dex)	[C/Fe] (dex)	[N/Fe] (dex)	[Mg/Fe] (dex)	[Ca/Fe] (dex)	[Ti/Fe] (dex)	[Cr/Fe] (dex)
in E269-66	-1.50 ± 0.2	-0.12 ± 0.2	0.25 ± 0.4	0.10 ± 0.2	0.00 ± 0.2	0.15 ± 0.3	0.15 ± 0.3
in KKs 3	-1.55 ± 0.2	-0.18 ± 0.2	0.45 ± 0.4	0.15 ± 0.2	0.30 ± 0.2	0.25 ± 0.3	0.05 ± 0.3
NGC 1904	-1.75 ± 0.2	0.03 ± 0.1	0.30 ± 0.3	0.25 ± 0.1	0.15 ± 0.1	0.15 ± 0.2	0.25 ± 0.2
NGC 5286	-1.75 ± 0.2	0.02 ± 0.1	0.35 ± 0.3	0.38 ± 0.1	0.25 ± 0.1	0.15 ± 0.2	0.25 ± 0.2
NGC 6254	-1.65 ± 0.2	-0.15 ± 0.1	0.25 ± 0.3	0.14 ± 0.1	0.12 ± 0.1	0.45 ± 0.2	-0.09 ± 0.2
NGC 6752	-1.75 ± 0.2	-0.06 ± 0.1	0.30 ± 0.3	0.22 ± 0.1	0.25 ± 0.1	0.20 ± 0.2	0.20 ± 0.2
NGC 7089	-1.75 ± 0.2	-0.01 ± 0.1	0.30 ± 0.3	0.35 ± 0.1	0.15 ± 0.1	0.20 ± 0.2	0.20 ± 0.2

and D2 and Fig. D1 demonstrate that several Galactic GCs from Sch05 with metallicities $[\text{Fe}/\text{H}] \sim -1.6$ dex and the two GCs in dSphs show similar indices within the measurement errors.

3.2.1 Comparison with literature data: abundances

Elemental abundances from literature high-resolution spectroscopic studies for five Galactic GCs are listed in Tables 5 and 6. It should be noted that our method yields systematically lower $[\text{Fe}/\text{H}]$ values by 0.1–0.15 dex (Table 4) for

Table 5. Elemental abundances in dex from literature high-resolution spectroscopic studies of red giant branch stars in five Galactic GCs analogous to the GCs in KKs3 and ESO 269-66.

NGC	[Fe/H]	[C/Fe]	[N/Fe]	[O/Fe]	[Na/Fe]	[Mg/Fe]	[Si/Fe]	[Ca/Fe]	[Ti/Fe]	[Cr/Fe]
1904 ^b	-1.58±0.12	–	–	0.10±0.19	0.32±0.25	0.26±0.07	0.28±0.03	0.22±0.04	0.22±0.10	-0.28±0.14
5286 ^a	-1.70±0.07 ^b	–	–	0.44±0.22	0.34±0.21	0.55±0.11	0.40±0.09	0.31±0.06	0.33±0.10	-0.05±0.20
6254 ^b	-1.53±0.06	-0.77±0.37	1.01±0.45	0.23±0.24	0.17±0.27	0.44±0.13	0.28±0.07	0.33±0.11	0.26±0.12	0.01±0.15
6752 ^b	-1.53±0.16	-0.45±0.37	0.93±0.63	0.26±0.25	0.32±0.26	0.38±0.15	0.47±0.19	0.31±0.09	0.20±0.11	-0.13±0.12
7089 ^c	-1.64±0.08 ^b	-0.62±0.14 ^b	–	0.42±0.16	0.06±0.23	0.38±0.08	0.40±0.01	0.28±0.02	0.17±0.02	-0.06±0.03

^a: Marino et al. (2015), ^b: Roediger et al. (2014), ^c: Six canonical RGB stars (r-only) by Yong et al. (2014).

Table 6. Elemental abundances in dex and their errors from literature high-resolution integrated-light spectroscopic studies for the two objects in common between our study and those of Colucci et al. (2017) (C17) and Larsen et al. (2017) (L17). Only [Fe/H] and the chemical elements common with the listed ones in Table 5 are shown. In the third row of the table, we present FeI and TiI abundances from the paper by C17 (marked by asterisk).

NGC	[Fe/H], σ	[Na/Fe], σ	[Mg/Fe], σ	[Si/Fe], σ	[Ca/Fe], σ	[Ti/Fe], σ	[Cr/Fe], σ
6254 ^{L17}	-1.481, 0.034	-0.038, 0.003	0.378, 0.067	–	0.380, 0.137	0.412, 0.097	0.104, 0.411
6752 ^{L17}	-1.883, 0.039	0.302, 0.023	0.391, 0.130	–	0.355, 0.114	0.342, 0.128	-0.101, 0.070
6752 ^{C17}	-1.58, 0.20*	0.04, 0.07	0.06, 0.07	0.40, 0.07	0.41, 0.04	0.39, 0.06*	-0.09, 0.09

Table 7. Comparison between the derived in this study and literature alpha-element ratios and ages for Galactic GCs. The table shows age from VandenBerg et al. (2013, V13) and $[\alpha/\text{Fe}]$ from Carretta et al. (2010, C10 and references therein) where $[\alpha/\text{Fe}]$ is the average of $[\text{Mg}/\text{Fe}]_{\text{max}}$, $[\text{Si}/\text{Fe}]_{\text{min}}$, and $[\text{Ca}/\text{Fe}]$. Our age estimate is equal for all five GCs: $\text{Age}_{\text{our}} = 12.6$ Gyr.

NGC	$[\alpha/\text{Fe}]^{\text{C10}}$ [dex]	$([\text{Ca}/\text{Fe}] + [\text{Mg}/\text{Fe}]')^{\text{our}}/2$ [dex]	Age^{V13} [Gyr]
1904	0.31	0.20±0.14	–
5286	–	0.32±0.14	12.50±0.38
6254	0.37	0.13±0.14	11.75±0.38
6752	0.43	0.24±0.14	12.50±0.25
7089	0.41	0.25±0.14	11.75±0.25

NGC 1904, 5286, 6752, and 7089 than the corresponding metallicities obtained in high-resolution spectroscopic studies of red giant branch stars in these GCs (Table 5). We suggest that this is the result of using i) the same microturbulent velocities for all stars in a cluster and ii) scaled-solar isochrones and model atmospheres. The method may yield biased results in case of non-solar peculiar chemical patterns. NGC 6254 shows a higher metallicity than other four Galactic GCs according to our analysis. However, it is not clear whether this may be due to the influence of Galactic field stars on the integrated spectrum of NGC 6254 (Sch05). Foreground reddening of NGC 6254 is strong. Additionally, a strong dust extinction gradient was detected within the cluster area (Leon et al. 2000).

Analysing the chemical compositions of the sample GCs, one has to take into account that all five considered Galactic GCs host multiple stellar populations in the sense

that their evolutionary sequences split in several components characterized by different Na, C, O, and He abundances (Piotto et al. 2015, Marino et al. 2015, Milone et al. 2013, 2015), and that their populations consist of several stellar generations characterized by correlated variations of light elements (Marino et al. 2015; Carretta et al. 2009, 2010; Fabbian et al. 2005). Variations of the abundances of Fe and s-process elements were detected in stars of NGC 5286 and NGC 7089 (Milone et al. 2015, Marino et al. 2015).

The following conclusions could be derived from the comparison of Tables 4 and 5: i) average abundances of RGB stars determined in high-resolution studies for a given element are similar within the errors for all five Galactic GCs; ii) when taking into account the measurement errors and a relatively small number of the RGB stars analysed in high-resolution studies, the mean medium-resolution and high-resolution abundances for a given element look similar for all five Galactic GCs for all of the considered elements except C and N; iii) abundances of Mg, Ca, Ti, and Cr look similar within the errors for the Galactic and two extragalactic GCs. Actually, there are slight systematic discrepancies between high and medium-resolution abundances of Mg and Ca for the Galactic GCs in Tables 4 and 5, although, the values of these differences are comparable with the corresponding errors of the abundance analysis. On average, RGB stars in our sample GCs appear to be more abundant in the light elements than the clusters' integrated light. A much stronger discrepancy was discovered for magnesium by Colucci et al. (2017).

The differences in the C and N abundances between RGB stars (Table 5) and the whole cluster (Table 4) may be interpreted as the result of an internal stellar evolution. The phenomenon of mixing within the atmospheres of RGB stars has long been studied (e.g. Kraft 1984, Gratton et al. 2012). The material processed through the CNO cycle in

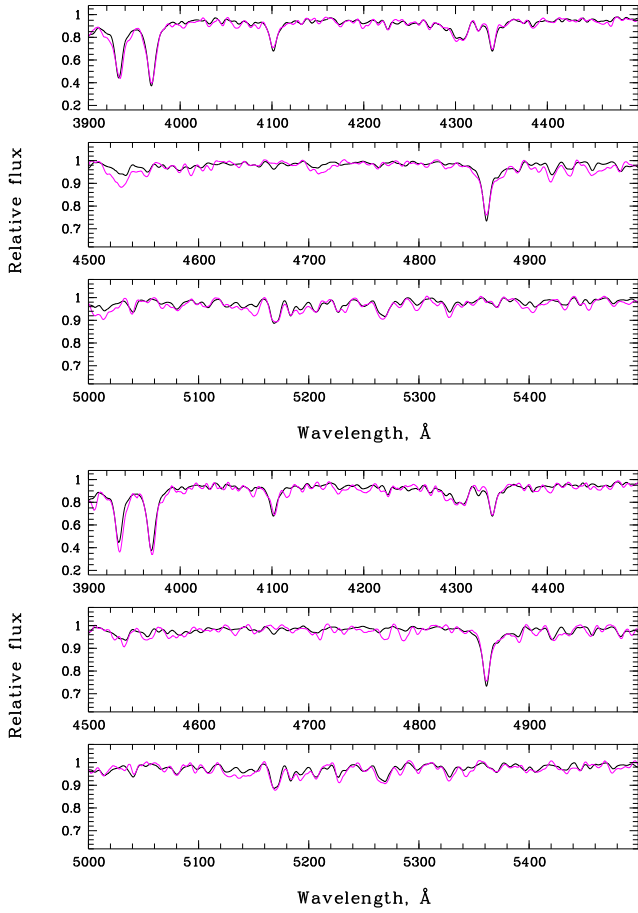


Figure 3. Continuum normalised spectra of GC in ESO 269-66 (top) and Kks3 (bottom) in comparison to the spectrum of NGC 5286 (black line) from Schiavon et al. (2005).

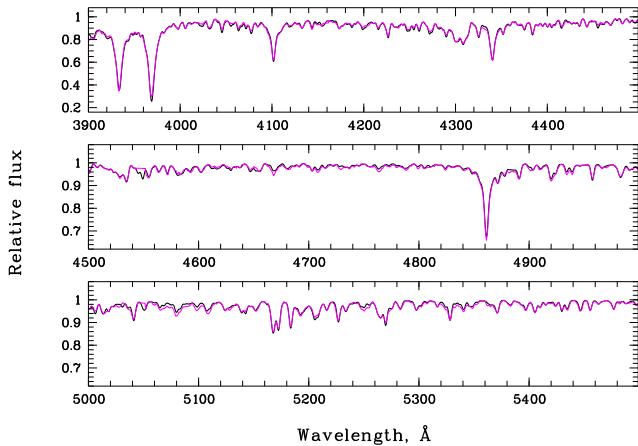


Figure 4. Continuum normalised spectrum of NGC 5286 from Schiavon et al. (2005) in comparison with the model one (black line) (please, see Table 4 and Section 3 for details).

the stellar interiors brings up to the photosphere by convective processes such as, for example, thermohaline mixing (Charbonnel & Zahn 2007). In this way, C and O are depleted and N is enhanced relative to stars on the Main Sequence, or the sub-giant branch. Oxygen is depleted to a much lesser extent than carbon (Carretta et al. 2005). According to the Chabrier (2005) mass function used by us in the calculation of the synthetic spectra of GCs, the radiation of RGB stars and that of MSTO stars comprise up to $\sim 30\%$ each of the total cluster optical light (please, see also Fig. 14 in Khamidullina et al. 2014). Therefore, at first glance the mentioned discrepancies do not look surprising. However, we measure C and N abundances average for a cluster using molecular bands which are more intensive in RGB stars. Please, note also the presence of several generations of stars in the sample objects differing by C, N, O, Na, and He. Pasquini et al. (2008) found an unpolluted MSTO star in NGC 6752 having $[N/Fe] = 0.32 \pm 0.1$ and $[O/Fe] = 0.24$. Unfortunately, there are no exhaustive data in the literature concerning the light-element abundances for MS stars in these GCs. The aforementioned slight differences between high and medium-resolution abundances of Mg and Ca for the Galactic GCs in Tables 4, 5 may also be caused by mixing within the atmospheres of RGB stars. Dissimilarities between abundances of chemical elements determined in high-resolution integrated-light analysis and spectroscopy of individual stars in GCs were revealed in the course of extensive studies of integrated-light spectra of many Galactic and extragalactic GCs (Colucci et al. 2017 and Larsen et al. 2017 and references therein). Future high-resolution studies of integrated-light spectra and of many stars with different masses, T_{eff} and $\log(g)$ in GCs will finally establish the values of the dissimilarities for different chemical elements.

3.2.2 Comparison with literature data: ages and Y

The knowledge of absolute ages and helium content of GCs is important for many reasons (e.g. VandenBerg et al. 2013, Charbonnel 2016). The ages of old Galactic GCs are measured with an accuracy of 1–2 Gyr and are model-dependent. Therefore, it would be instructive to compare the results of deep photometric and spectroscopic studies to achieve better accuracies. Age and He abundance are the second and the third parameters (the first being metallicity) defining the distribution of stars on the HB of GCs (Gratton et al. 2010). Helium content is one of the main factors influencing evolution of stars. In particular, only about 30% of stars in GCs at the ages of 12 Gyrs, are the first generation stars. Helium abundance is higher in stars belonging to the second and subsequent (if any) stellar generations in GCs. Large variations in He abundance in GCs are correlated with the variations of Na, O, and other elements (D’Antona et al. 2002). He-enriched stars evolve faster at a given age. At the MSTO such stars are less massive than the He-poor ones. “Variations in the median He abundance allow to explain the extremely blue HB of GCs like NGC 6254 (=M 10) and NGC 1904 (=M 79)...” (Gratton et al. 2010).

The literature $[\alpha/Fe]$ values from Carretta et al. (2010) and ages from VandenBerg et al. (2013) are summarised in Table 7 together with our results. Carretta et al. (2010) used the average of the maximum Mg abundance ($[Mg/Fe]_{\text{max}}$), minimum Si abundance ($[Si/Fe]_{\text{min}}$), and $[Ca/Fe]$ as a mea-

Table 8. Contribution of HB stars to the integrated light of the cluster in the B-band with respect to the corresponding contribution of RGB stars brighter than the level of HB ($I_{\text{HB}}/I_{\text{RGB}}$). These values are shown for five Galactic GCs (CMDs in Fig. 5) and for synthetic spectra of GCs computed using isochrones from B08: (1) $Z = 0.0004$, $\log(\text{age}) = 10.1$, $Y = 0.3$, (2) $Z = 0.0004$, $\log(\text{age}) = 10.05$, $Y = 0.3$, (3) $Z = 0.0004$, $\log(\text{age}) = 10.1$, $Y = 0.26$ and (4) $Z = 0.0004$, $\log(\text{age}) = 10.05$, $Y = 0.26$ (please, see text for details). The stars belonging to HBs and RGBs of Galactic GCs were selected as it is demonstrated in Fig. 5.

	NGC 1904	NGC 5286	NGC 6254	NGC 6752	NGC 7089	1	2	3	4
$I_{\text{HB}}/I_{\text{RGB}}$	0.85	0.79	0.79	0.8	0.78	0.77	0.47	0.65	0.54

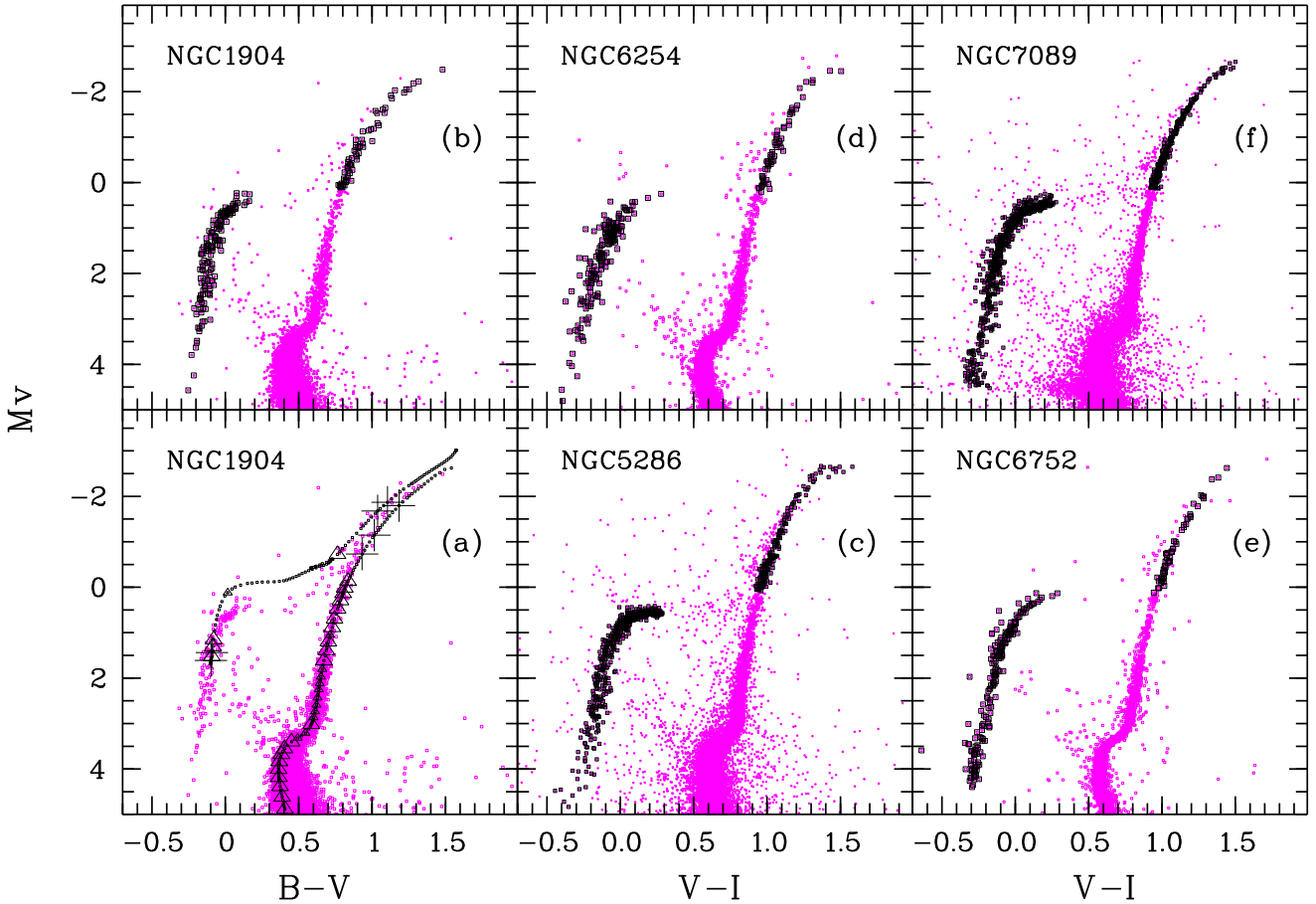


Figure 5. (a): CMD of NGC 1904 (Piotto et al. 2002) and the overplotted isochrone $Z = 0.0004$, $Y = 0.30$ and $\log(\text{Age}) = 10.10$ (B08). Evolutionary stages contributing to the total cluster’s light less than 1%, 1–3% and more than 3% are shown as small triangles, large triangles, and big crosses respectively (Section 3.2.2). (b–e) Selection of HB and RGB stars using deep HST CMDs from Sarajedini et al. (2007) and Piotto et al. (2002).

sure of the over-abundance of α -elements, because this parameter coupled with $[\text{Fe}/\text{H}]$ and several other abundances describes well the chemical composition of the primordial population in GCs. It is seen that all the GCs have EHBs and old age (~ 12 Gyr) (e.g. VandenBerg et al. 2013). Light-element content of their RGB stars is enhanced, $[\alpha/\text{Fe}] \sim 0.4$ (Carretta et al. 2010 and references therein). Table 7 illustrates a pretty good agreement between the literature high-resolution spectroscopic and deep photometric data and our results that are based on the analysis of medium-resolution spectra.

In the following, we will focus on some details of our procedure of age and Y determination to better understand the reasons of the existing discrepancies between the data derived using different methods (Table 7). Figure 2 shows the differences in shapes and depths of three Balmer lines in the integrated synthetic spectra of a GC computed using the method described in Section 3.1, abundances of NGC 5286 (Table 4) and different isochrones by B08. For this presentation, we select only four isochrones providing the best agreement between the synthetic and the observed spectra. The synthetic Balmer lines computed with several

other isochrones ($\log(\text{Age}) = 10.15$, $Y = 0.30$, $Z = 0.0004$, $\log(\text{Age}) = 10.15$, $Y = 0.26$, $Z = 0.0004$) are shown in Appendix A (Fig. A1). Figure A2 illustrates the comparison of the Balmer lines in the spectra of NGC 5286, 1904, 6254, 6752, and 7089.

Figs 2 and A1 (Appendix A) show that the cores and wings of the lines are fitted better in case we choose the isochrone (B08): $Z = 0.0004$, $\log(\text{Age}) = 10.10$, $Y = 0.30$.

Figure 2 demonstrates that the depths of the Balmer lines in the presented synthetic spectra differ only by 1-2% (Fig. 2), when we use four different isochrones with the ages 12.6 Gyr and 11.2 Gyr and helium abundances $Y = 0.26$ and 0.3. The quality of observational data determines the uncertainties of age and Y . It is worth mentioning that the Balmer lines are blended in the medium resolution spectra, and different chemical elements (primarily Fe) re-shape their wings. For example, Khamidullina et al. (2014) selected the best-fitting isochrone for NGC 6254: $Z = 0.0004$, $\log(\text{Age}) = 10.05$, $Y = 0.30$ (B08). VandenBerg et al. (2013) determined for NGC 6254: $[\text{Fe}/\text{H}] = -1.57$, $Y = 0.25$ and the absolute age 11.75 Gyr. The last age estimate is between our result (Table 7) and that of Khamidullina et al. (2014).

3.2.3 CMDs of five Galactic GCs in comparison with theoretical isochrones

In this section, we will address the question: why the isochrone $Z = 0.0004$, $\log(\text{Age}) = 10.10$, $Y = 0.30$ describes reasonably well the intensities and shapes of Balmer lines in the medium-resolution integrated-light spectra of our sample Galactic GCs, while it is known that our sample GCs possess multiple stellar populations, and their HB morphologies can not be fully reproduced by an isochrone that is for a single Y value only.

Figure 5 shows the CMDs of five Galactic GCs. We used the deep CMD of NGC 1904 from Piotto et al. (2002). Other high-quality photometric data were taken from the paper by Sarajedini et al. (2007). Figure 5a illustrates our method of synthetic integrated-light spectra calculation (Section 3.1 and references therein) and compares the CMD of NGC 1904 with the isochrone $Z = 0.0004$, $\log(\text{Age}) = 10.10$, $Y = 0.30$ (B08). One can see that the theoretical HB appears to be significantly more luminous than the level of the observed HB. The same situation takes place for other four GCs, because the levels of the observational HBs look similar. The structures of the observed HBs are complex (e.g. Marino et al. 2015 and references therein, Schiavon et al. 2004). They can not be exhaustively described by any theoretical isochrone.

Table 8 presents the contribution of HB stars to the integrated light of the clusters in the B-band of the Johnson-Cousins photometric system divided by the corresponding contribution of RGB stars brighter than the level of the HB. The lower luminosity level chosen to select RGB stars corresponds to the local maxima of luminosity on the RGB (B08). Figs 5(b)–(e) illustrate the way how the stars belonging to the HB and upper RGB of GCs have been selected. We used the B-band, because its wavelength coverage is close to the analysed spectral range (Section 3.1). We transformed stellar photometric data corrected for foreground extinction into the B-band as follows: $(V - I)_0 = 0.893(B - V)_0$. We obtained this formula for photometric standard stars (Landolt, 1992).

The values in the last four columns of Table 8 represent the theoretical contribution of HB stars to the integrated spectra of GCs computed using our method (Section 3.1 and references therein) with respect to the corresponding contribution of upper RGB stars. Theoretical contribution of a particular isochrone point to the total luminosity of the cluster was calculated for the selected four isochrones from B08 using the mass function by Chabrier (2005). Evolutionary stages (points of isochrones) with initial stellar masses differing by less than $10^{-4} M_\odot$ were excluded from the calculations of synthetic integrated-light spectra of GCs.

One can conclude from Table 8 that the contribution of HB stars to the integrated spectra of our sample GCs with respect to the corresponding contribution of RGB stars brighter than the level of HB is reproduced well by the isochrone $\log(\text{Age}) = 10.10$, $Y = 0.30$, $Z = 0.0004$ (B08).

To summarise, the integrated-light synthetic spectra calculated using one isochrone can fit particularly well the observed integrated-light medium-resolution spectra of GCs, when the following conditions are satisfied: i) the range of stellar colours (effective temperatures) covered by the theoretical HB agrees well with the corresponding observational data; ii) contribution of the HB integrated light to the total luminosity of the cluster is similar in the observational photometric and spectroscopic data, on the one hand, and in the integrated-light synthetic spectra calculated using this isochrone, on the other hand.

4 STRUCTURE OF THE GLOBULAR CLUSTER IN KKS 3

Two 1200 s exposures obtained aboard the HST with the Advanced camera for surveys (ACS) and the filters F606W and F814W (SNAP program 13442) were used to derive structural parameters of the GC in KKS 3. A fragment of the image containing the GC is shown in Fig. 6. The azimuthally-averaged surface brightness profiles of the central region of the galaxy including the GC was generated using aperture photometry with circular apertures of increasing size on the F606W and F814W frames using the SURFPHOT program in the MIDAS package developed by ESO. Bright foreground stars and background galaxies were masked. The centre of the cluster was determined with an accuracy of ~ 1 pixel in each coordinate using the MIDAS routine FIT/ELL3. The background was defined by fitting a plane to the image with the FIT/BACKGROUND program. Conversion from the instrumental photometric system to the V and I bands of the Johnson-Cousins system was carried out using zeropoints and calibration coefficients from Sirianni et al. (2005).

The integrated magnitudes of the cluster in the V and I bands were estimated to be $V = 18.41 \pm 0.03$ and $I = 17.45 \pm 0.05$ yielding the colour $V - I = 0.96 \pm 0.06$. These results stay in good agreement with the estimates by Karachentsev et al. (2015b). Please, note that the presence of a bright red star $\sim 9''$ to the South-West from the GC can influence surface photometry results. The surface brightness profiles of the central region of KKS 3 are shown in Fig. 7(a). The King (1962) profiles with the parameters listed in Table 9 the V and I bands are over-plotted. The models were fitted after subtraction of the galactic contri-

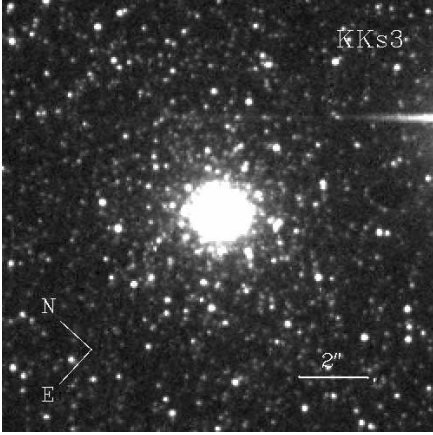


Figure 6. F606W ACS image of the central GC in KKS3

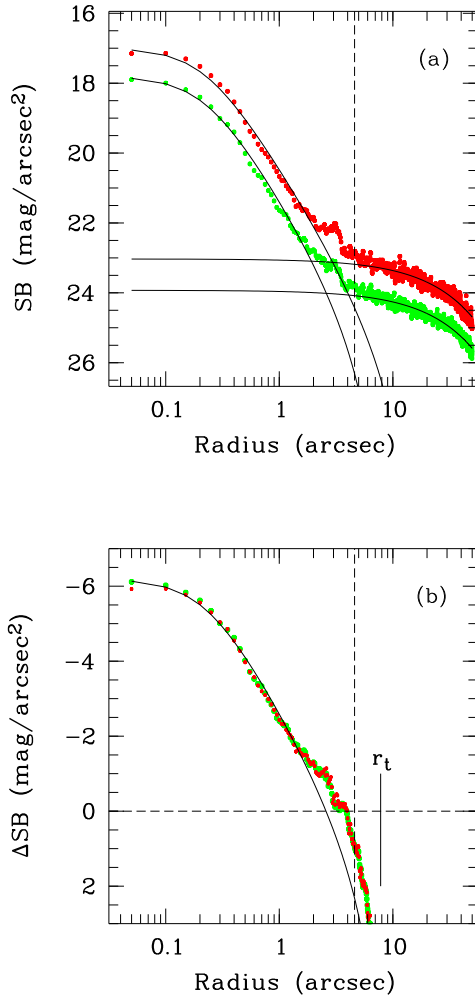


Figure 7. (a): Azimuthally-averaged surface brightness profiles of the central region of KKS3 in the V and I bands (dots). Solid lines show a decomposition of the profile inside the fit range represented by the exponential function and the King (1962) law. (b): The same as in (a), but after subtraction of the galactic contribution. The horizontal dashed line is a zero line. The vertical dashed line in panels (a) and (b) marks the radius ($R \sim 4.6''$) at which the galactic contribution begins to prevail.

Table 9. Structural parameters of GC in KKS3 measured using the the King (1962) law: central surface brightness in mag arcsec^{-2} , core and tidal radii in arcsec.

μ_V^0	μ_I^0	r_c	r_t
17.74 ± 0.02	16.97 ± 0.02	0.22 ± 0.01	7.8 ± 4.7

bution. The last one was estimated by fitting the exponential law to the azimuthally-averaged surface brightness profiles with the parameters from Karachentsev et al. (2015a).

After subtraction of the galactic contribution, it becomes clear that there is brightness excess along the measured surface brightness profile at the radii between $2''$ and $4.6''$ reaching $\sim 8\sigma$ above the background (Fig. 7b), where σ is the dispersion of sky counts at the radii greater than r_t after subtraction of the galactic contribution: a mean $\sigma \sim 0.13$ mag. The mentioned "extra" light constitutes $\sim 10\%$ of the total cluster luminosity integrated from the centre to the tidal radius.

Our photometric results yield the half-light radius of the cluster $r_h = 4.8 \pm 0.2$ pc. The object appears to be a bit more diffuse than the GC in ESO 269-66 and than the five Galactic GCs with similar spectra (Table 7). The concentration parameter $c = \log(r_t/r_c) = 1.6$ of the GC in KKS3 is typical for massive Galactic GCs (Harris, 1996).

5 DISCUSSION

5.1 Multiple stellar populations in the nuclei of ESO 269-66 and KKS3?

As it was noted in Section 3.2.1, according to the literature studies, all five Galactic counterparts of the two nuclei of dSphs exhibit the signs of multiple stellar populations in the sense of splits of their evolutionary sequences, correlated variations of light-element abundances coupled with He enrichment and the appearance of EHBs populations. NGC 5286 and 7089 are anomalous GCs (Marino et al. 2015 and references therein). Can we find more analogues of the GCs in KKS3 and ESO 269-66 using publicly available spectral data?

A new WiFeS Atlas of Galactic Globular cluster Spectra (WAGGS) (Usher et al. 2017) provides 22 integrated-light spectra of GCs in the Milky Way satellites and of 64 old Galactic GCs. This survey includes five objects of our study (NGC 1904, 5286, 6254, 6752, 7089) and a dozen other GCs with $[\text{Fe}/\text{H}] \sim -1.6$ dex. Two Large Magellanic Cloud GCs in this sample, NGC1786 and NGC1916, have similar metallicities and old ages (Usher et al. 2017 and references therein). We compared the spectra of all these objects using the WAGGS spectrum of NGC 5286 as a reference one. We used the original resolution ($R = 6800$) and all four gratings that cover the total spectral range: $3300 - 9050\text{\AA}$. WAGGS contains repeated observations for some GCs. We used spectra having higher signal-to-noise ratio. The results of the comparison are presented in Fig. 8 and at an any-

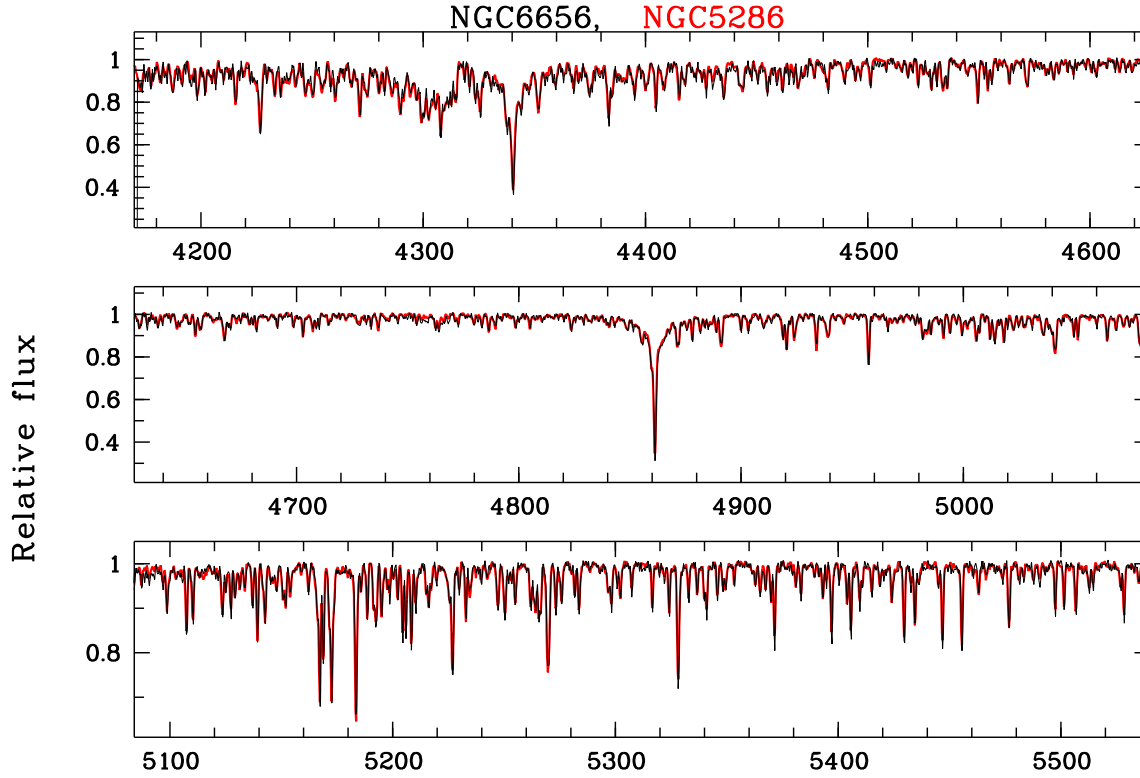


Figure 8. Normalised spectra of NGC 5286 (red in the electronic edition) and NGC 6656 (black) from WAGGS (Usher et al. 2017).

mous ftp website⁴. The comparison plots do not include the parts of the spectra distorted by strong telluric lines.

As a result, we found three additional GCs with integrated-light spectra similar to those of the GCs in Kks 3 and ESO 269-66: NGC 6656, 6273, and 6681. The depths and shapes of Balmer and FeI, II lines, molecular bands (CH, MgH, and CN), strong CaI, CaII, and MgI lines (CaII H+K, CaII 8498, 8542, 8662Å, CaI 4227Å, and MgI 5183Å), and of weaker lines and blends contributed by different chemical elements look similar to the corresponding spectroscopic features in the WAGGS spectrum of NGC 5286. On the other hand, NGC 6254 looks a bit more metal-rich than NGC 5286. The same trend was discovered in Section 3.2 (please, see also Larsen et al. 2017). The spectrum of NGC 5139 (ω Cen) also demonstrates resemblance to the spectrum of NGC 5286. However, Fe lines look $\sim 1 \div 2\%$ less intensive in the spectrum of NGC 5139. Johnson et al. (2017) reported on the close identity of Fe I and Fe II line profiles of stars in three metallicity groups belonging to NGC 5139 and NGC 6723 with similar T_{eff} , $\log(g)$, and $[\text{Fe}/\text{H}]$. We suggest that determination of ages and Y and accurate abundance analysis for the found GCs with similar spectra is a subject of a separate study.

To summarise, all five known Fe-complex Galactic GCs with $[\text{Fe}/\text{H}] \sim -1.6$ dex (Marino et al. 2015, Johnson et al. 2017) have medium-resolution spectra resembling the spectra of GCs in Kks 3 and ESO 269-66: NGC 5286, 7089, 6656,

Table 10. Properties of the selected Galactic GCs (please see text for details). Fe-complex GCs (Marino et al. 2015, Johnson et al. 2017) are marked by asterisk.

NGC	D_{MW} (2)	Z (3)	$E(B-V)$ (4)	M_{V0} (5)	HBR (6)	R_h (7)	$[\text{Fe}/\text{H}]$ (8)
1904	18.8	-6.3	0.01	-8.23	0.89	3.00	-1.58
5286*	8.4	2.0	0.24	-9.45	0.80	2.21	-1.70
6254	4.6	1.7	0.28	-8.34	0.98	2.32	-1.57
6752	5.2	-1.7	0.04	-7.85	1.00	2.72	-1.55
7089*	10.4	-6.7	0.06	-9.21	0.96	3.11	-1.66
5139*	6.4	1.4	0.12	-10.63	—	6.44	-1.64
6273*	1.6	1.4	0.38	-10.29	—	3.13	-1.76
6656*	4.9	-0.4	0.34	-9.54	0.91	3.03	-1.70
6681	2.1	-1.9	0.07	-7.33	0.96	2.43	-1.62

6273 and 5139. All nine possible Galactic analogues of the GCs in Kks 3 and ESO 269-66 demonstrate the signs of multiple stellar populations (Piotto et al. 2015; Milone et al. 2013, 2015; Marino et al. 2015; Carretta et al. 2009, 2010; Fabbian et al. 2005; O’Malley et al. 2017). Please note, that the discovered resemblance of the spectra is surprising, because integrated-light spectra can be influenced by the Galactic field contamination and by effects of stochastic fluctuations in a number of stars within the spectrograph field-of-view.

Properties of the objects with the spectra similar to the spectra of Kks 3 and ESO 269-66 are summarised in Table 10. The columns are the following: (2-6) distance from the Galactic centre (kpc), Z distance component toward the

⁴ <ftp://ftp.sao.ru/pub/sme/TwoDSphs/AppendixF.pdf>

North Galactic pole (kpc), colour excess (mag), absolute magnitude (mag), and HB ratio ($HBR = (B - R)/(B + V + R)$) from Harris (1996), (7) half-light radius (pc) from Mackey & van den Bergh (2005), (8) $[Fe/H]$ (dex) from Carretta et al. (2010 and references therein). One may conclude that the listed objects are among the brightest GCs in our Galaxy. They have low metallicity $[Fe/H] \sim -1.6$ dex and old age (e.g. Carretta et al. 2010, VandenBerg et al. 2013). All the GCs, except for ω Cen, have similar half-light radii $R_h = 2.7 \pm 0.3$ pc and extended blue HBs (Piotto et al. 2015).

The objects listed in Table 10 do not form an ensemble belonging to any known Galactic tidal stream (Grillmair & Carlin 2016), although some of them are thought to be associated with streams (e.g. Bellazzini et al. 2003, Penarrubia et al. 2005). Low Galactic latitudes and Z distance components of the GCs may indicate that they have participated in the process of the Galactic thick disk build-up. Six of the sample GCs were classified as disk/bulge objects by Carretta et al. (2010) basing on observations of thousands of stars in GCs. The thick disk is composed mostly of old stars and dominates the stellar number density between one and five kpc above the Galactic plane (Gilmore & Reid 1983). Future high-resolution observations of many stars with different masses, T_{eff} and $\log(g)$ and accurate comparison of chemical abundances of stars in the sample GCs, dSphs, and the thick Galactic disk will help to make conclusions concerning the origin of these cosmological structures.

5.2 On the origin of KKs 3 and of its nucleus

Early-type dwarf galaxies are usually situated in close vicinity of giant neighbours. Their morphologies are strongly influenced by environmental processes. What is then the origin of KKs 3 and of its nucleus? KKs 3 is located far from nearby massive galaxies and from the Local Void whose expansion does not affect the motion of the galaxy (Karachentsev et al. 2015a). If KKs 3 is not a runaway object from the Local group, it is probably a remnant of collision of two or three small galaxies (e.g. Väisänen et al. 2014). Pairs and triplets of small galaxies are found in different environments (e.g. Argudo-Fernandez et al. 2015 and references therein). Three star forming episodes in KKs 3 might be the evidences of these events. Katkov, Kniazev & Sil'chenko (2015) considered ionized gas accretion and satellite merging as the most probable explanation for the results of their studies of kinematics and metallicity of gas in several isolated S0s. Objects with small old or active nuclei are ubiquitous among low mass spiral galaxies. If KKs 3 is a low-mass analogue of S0s (Kormendy & Bender 2012), its occurrence in a very rarefied environment is not surprising. There is a large number of brighter lenticular galaxies in the field (e.g. Sulentic et al. 2006). The mass of gas involving in a collision event determines the duration and the intensity of star formation in the galactic centre. Observations show that galactic nuclear activity is a main driver of morphological transformation of intermediate-mass early-type galaxies in any environments and that the galactic surface mass densities, concentration indexes, and luminosities of galactic nuclei grow with the corresponding galaxy mass (Kauffmann et al. 2003, Argudo-Fernandez et al. 2016).

There are many details to be added on, but we consider this issue to be a matter of a separate study.

6 CONCLUDING REMARKS

In this paper, we analysed properties of stellar populations of nuclear star clusters in two dwarf spheroidal galaxies situated in very different environments: a unique isolated dSph KKS3 discovered by Karachentsev et al. (2015b) and ESO 269-66, a close dSph neighbour of Cen A (Karachentsev et al. 2007). The galaxies have similar star formation histories and mean stellar metallicities.

We estimated ages, helium abundance (Y), $[Fe/H]$, and abundances of C, N, Ca, Mg, Ti, and Cr for the nuclei using their medium-resolution spectra acquired with the Robert Stobie Spectrograph at the Southern African Large Telescope. To perform this work, we employed our developing method (Sharina et al. 2013, Khamidullina et al. 2014, Sharina et al. 2014) of computation of integrated-light synthetic spectra of GCs using models of stellar atmospheres according to the mass function by Chabrier (2005) and stellar parameters defined by the selected isochrone from the paper by B08. The derived age of 12.6 Gyr, $Y=0.3$, $[Fe/H] \sim 1.5 \div 1.55$ dex and abundances of chemical elements appear to be in the agreement with the corresponding data for five Galactic GCs from the sample of Sch05: NGC 1904, 5286, 6254, 6752, and 7089. Ages and elemental abundances for the Galactic GCs were estimated using our method and medium-resolution spectra from the library of Sch05. The average abundances of chemical elements from the high-resolution literature spectroscopic studies for the considered Galactic GCs confirm our findings concerning the similarity.

Additionally, we found four objects in WAGGS (Usher et al. 2017) with integrated-light spectra resembling the WAGGS spectra of the five Galactic counterparts of the GCs in KKs 3 and ESO 269-66. The objects are: NGC 6273, 6656, 6681, and 5139. Determination of ages and Y and accurate abundance analysis for these GCs is a subject of a separate study.

Eight of the selected Galactic analogues of the GCs in KKS3 and ESO 269-66 (Table 10), possess extended blue HBs, correlated variations of light elements, and splits of evolutionary sequences (Piotto et al. 2015, Milone et al. 2013, 2015; Marino et al. 2015, Carretta et al. 2010, Fabbian et al. 2005, O'Malley et al. 2017). The ninth GC with the similar WAGGS spectrum, NGC 6681, overlaps the main body of Sagittarius dSph. Five of the found counterparts are iron-complex GCs: NGC 5286, 7089, 6273, 6656, and 5139 (Marino et al. 2015 and references therein, Johnson et al. 2017).

All the selected Galactic analogues of our two nuclei are at the extreme high end of the GC mass function. All of them, except NGC 5139 (ω Cen), have similar half-light radii ($R_h = 2.7 \pm 0.3$). The GC in ESO 269-66 is exactly of the same size (Georgiev et al. 2009). The GC in KKs 3 is slightly more extended ($r_h = 4.8 \pm 0.2$ pc) according to our measurements using HST images. There is brightness excess near the end of the surface brightness profile of this cluster which is not described by the King (1962) law. This "extra"-light constitutes $\sim 10\%$ of the total cluster luminosity.

One may conclude that our method described in Section 3.1 is capable to select GCs with EHBs, most of which are very massive and some of which belong to a rare class of anomalous GCs. It is intriguing that GCs as the witnesses of most powerful star forming episodes in galaxies show similar properties of stellar populations independent on the environments.

7 ACKNOWLEDGEMENTS

We thank the anonymous referee for comments that helped to improve the paper. All spectroscopic observations reported in this paper were obtained with the Southern African Large Telescope (SALT) under programmes 2010-1-RSA_OTH-002 and 2014-2-MLT-001 (PI: Kniazev). The work is performed under the support of the grant of the Russian Science Foundation 14-12-00965 and in compliance with the Russian Government Program of Competitive Growth of Kazan Federal University. A.K. acknowledges support from the National Research Foundation (NRF) of South Africa and from the Russian Science Foundation (project no. 14-50-00043). We thank L.N. Makarova for providing us stellar photometric data for KKs3. The work is based on observations made with the NASA/ESA Hubble Space Telescope. STScI is operated by the Association of Universities for Research in Astronomy, Inc. under NASA contract NAS 526555.

REFERENCES

- Argudo-Fernandez M., Shen S., J. Sabater J., Duarte Puer-tas S., S. Verley S., Yan X., 2016, *A&A* 592, 30
- Argudo-Fernandez M., et al., 2015, *A&A* 578, 110
- Bellazzini M., Ferraro F.R., Ibata R., 2003, *AJ*, 125, 188
- Bekki, K.; Norris J.E., 2006, *ApJ*, 637, L109
- Bertelli G., Girardi L.; Marigo P., Nasi E., 2008, *A&A*, 484, 815 (B08)
- Buckley D. A. H., Swart G. P., Meiring J. G., 2006, in Stepp L. M., ed., *SPIE Proc. Vol. 6267, Ground-based and Airborne Telescopes*. SPIE, Bellingham, p. 62670Z
- Burgh E. B. et al. 2003, in Iye M., Moorwood A. F. M., eds, *SPIE Proc. Vol. 4841, Instrument Design and Performance for Optical/Infrared Ground-based Telescopes*. SPIE, Bellingham, p. 1463
- Burstein, D.; Faber, S. M.; Gaskell, C. M.; Krumm, N., 1984, *ApJ*, 287, 586
- Carretta, E.; Bragaglia, A.; Gratton, R. G.; Recio-Blanco, A.; Lucatello, S.; D’Orazi, V.; Cassisi, S., 2010, *A&A*, 516, 55
- Carretta E.; Bragaglia A.; Gratton R.; Lucatello S., 2009, *A&A*, 505, 139
- Carretta, E.; Gratton, R. G.; Lucatello, S.; Bragaglia, A.; Bonifacio, P., 2005, *A&A*, 433, 597
- Castelli F., Kurucz R. L., 2003, in N. Piskunov et al. eds., *Proc. IAU Symp. 210: Modeling of Stellar Atmospheres*, Kluwer, Dordrecht, p. A20
- Chabrier G., 2005, *The initial mass function 50 years later*, *Astrophysics and Space Science Library*, 327, 41
- Chantreau W., Charbonnel C., Meynet G., 2016, *A&A* 592, 111
- Charbonnel, C., 2016, in *Stellar Clusters: Benchmarks of Stellar Physics and Galactic Evolution - EES2015*, Moraux E. and Lebreton Y. and Charbonnel C. eds., *EAS Publications Series*, Vol. 80, p. 177
- Charbonnel, C., Zahn, J.-P. 2007, *A&A*, 467, L15
- Colucci J.E., Bernstein R.A., McWilliam A., 2017, *ApJ*, 834, 105
- Côté, et al., 2006, *ApJS*, 165, 57
- Crawford S. M. et al. 2010, in Silva D. R., Peck A. B., Soifer B. T., eds, *SPIE Proc. Vol. 7737, Observatory Operations: Strategies, Processes, and Systems III*. Am. Inst. Phys., New York, p. 773725
- Crnojević, D. et al., 2016, *ApJ*, 823, 19
- Crnojević, D.; Rejkuba, M.; Grebel, E. K.; da Costa, G.; Jerjen, H., 2011, *A&A*, 530, 58
- D’Antona F., Caloi V., Montalbán J., Ventura P., Gratton R., 2002, *A&A*, 395, 69
- Da Costa G. S., Grebel E. K., Jerjen H., Rejkuba M., Sharina M. E., 2009, *AJ*, 137, 4361
- Dias B. et al., 2015, *A&A*, 573, 13
- Dolphin A.E., 2002, *MNRAS*, 332, 91
- Fabbian D., Recio-Blanco A., Gratton R. G., Piotto G., 2005, *A&A* 434, 235
- Georgiev I.Y., Hilker M., Puzia T.H., Goudfrooij P., Baumgardt H., 2009, *MNRAS*, 396, 1075
- Gilmore G., Reid N., 1983, *MNRAS*, 202, 1025
- Gratton, R. G., Carretta, E., Bragaglia, A., 2012, *A&ARv*, 20, 50
- Gratton R. G., Carretta E., Bragaglia A., Lucatello S., D’Orazi, V., 2010, *A&A*, 517, 81
- Grillmair, C.J., Carlin J.L., 2016, in Newberg H.J. & Carlin J.L., eds., *Astrophysics and Space Science Library*, Vol 420., *Tidal Streams in the Local Group and Beyond*, Springer, Switzerland, p.87
- Harris W.E., 1996, *AJ*, 112, 1487 (2010 edition)
- Johnson C.I., Caldwell N., Rich R.M., Mateo M., Bailey III J.I., Clarkson W.I., Olszewski E.W., Walker M.G., 2017, *ApJ* 836, 168
- Karachentsev I. D., Kniazev A. Yu., Sharina M. E., 2015a, *AN*, 336, 707
- Karachentsev I. D., Makarova L. N., Makarov D. I., Tully R. B., Rizzi L., 2015b, *MNRAS*, 447, L85
- Karachentsev, I.D.; Makarov, D.I.; Kaisina, E.I., 2013, *AJ*, 145, 101
- Karachentsev I. D., et al., 2007, *AJ*, 133, 504
- Karachentsev I. D., Karachentseva V. E., Sharina M. E., 2005, *IAU Colloq. 198: Near-fields cosmology with dwarf elliptical galaxies*, eds. Jerjen H. and Binggeli B., 295
- Katkov I.Yu.; Kniazev A.Yu.; Sil’chenko O.K., 2015, *AJ*, 150, 24
- Kauffmann, et al., 2003, *MNRAS*, 346, 1055
- Khamidullina D. A., Sharina M. E., Shimansky V. V., Davoust, E., 2014, *Astrophysical Bulletin*, 69, 409
- King I., 1962, *AJ*, 67, 471
- Kniazev A. Y. et al., 2008, *MNRAS*, 388, 1667
- Kobulnicky H.A.; Nordsieck K.H.; Burgh E.B.; Smith M. P.; Percival J.W.; Williams T.B.; O’Donoghue D., 2003, in Iye M. and Moorwood A. F. M. eds., *SPIE Proc. Vol. 4841, Instrument Design and Performance for Optical/Infrared Ground-based Telescopes*, SPIE, Bellingham, p. 1634
- Kormendy J., Bender R., 2012, *ApJS*, 198, 2
- Kraft R. P., 1984, *PASP*, 106, 553

- Kurucz R. L., 1994, CD-Room No. 19-22, Cambridge, Mass., SAO
- Landolt A.U., 1992, *AJ*, 104, 340
- Lardo, C., et al., 2016, *A&A*, 585, 70
- Larsen S. S.; Brodie J. P.; Strader J., 2017, *A&A*, 601, 96
- Larsen, S. S.; Strader, J.; Brodie, J. P., 2012, *A&A*, 546, 53
- Leigh N.; Böker T.; Knigge, C., 2012, *MNRAS*, 424, 2130
- Leon, S.; Meylan, G.; Combes, F., 2000, *A&A*, 359, 907
- Lotz J.M., Miller B.W., Ferguson H.C., 2004, *ApJ*, 613, 262
- Mackey A.D. & van den Bergh S., 2005, *MNRAS* 360, 631
- Makarova L., et al. 2007, *Proceedings IAU Symposium 235: Galaxy Evolution across the Hubble Time*, Eds. F.Combes and J.Palouš, 320
- Malavolta L., Sneden C., Piotto G., Milone A.P., Bedin L.R., Nascimbeni V., 2014, *AJ*, 147, 25
- Marino A.F. et al., 2015, *MNRAS*, 450, 815
- Marino A.F. et al., 2008, *A&A*, 490, 625
- Milone A.P., et al., 2015, *MNRAS*, 447, 927
- Milone A.P. et al., 2013, *ApJ*, 767, 120
- O'Donoghue D., et al., 2006, *MNRAS*, 372, 1510
- O'Malley E.M., Kniazev A., McWilliam A., Chaboyer B., 2017, *ApJ* accepted, eprint arXiv:1706.06962
- Pasquini, L.; Ecuivillon, A.; Bonifacio, P.; Wolff, B., 2008, *A&A*, 489, 315
- Peñarrubia et al., 2005, *ApJ*, 626, 128
- Piotto G., et al. 2015, *AJ*, 149, 91
- Piotto G., et al. 2002, *A&A*, 391, 945
- Roediger J.C., Courteau S., Graves G., Schiavon R.P, 2014, *ApJS*, 210, 10 (R14)
- Salaris M.; Weiss A.; Ferguson J.W.; Fusilier D.J., 2006, *ApJ*, 645, 1131
- Sarajedini A., et al., 2007, *AJ*, 133, 1658
- Schiavon R.P., Caldwell N.M., Heather H.P.; Courteau S., MacArthur L.A., Graves G.J., 2012, *AJ*, 143, 14
- Schiavon R.P., Rose J.A., Courteau S., MacArthur L.A., 2005, *ApJS*, 160, 163
- Schiavon R.P., Rose J.A., Courteau S., MacArthur L.A., 2004, *ApJ*, 608, L33
- Sharina M. E., Donzelli C. J., Davoust E., Shimansky V. V., Charbonnel C., 2014, *A&A*, 570, 48
- Sharina M. E., Shimansky V. V., Davoust E., 2013, *Astronomy Reports*, 57, 410
- Sharina M. E., et al., 2008, *MNRAS*, 384, 1544
- Sharina M. E., Puzia T. H., Makarov D. I., 2005, *A&A*, 442, 85
- Sirianni M., Lee M.J., Benitez N., et al., 2005, *PASP*, 117, 1049
- Sulentic, J. W., et al., 2006, *A&A*, 449, 937
- Thomas D., Maraston C., Johansson J., 2011, *MNRAS*, 412, 2183
- Thomas D., Maraston C., Korn A., 2004, *MNRAS*, 351, L19
- Thomas D., Maraston C., Bender R., 2003, *MNRAS*, 343, 279
- Thomson, R.C., 1992, *MNRAS*, 257, 689
- Trager S. C., Worthey G., Faber S. M., Burstein D., Gonzalez J. J., 1998, *ApJS*, 116, 1
- Usher C., et al. 2017, *MNRAS*, 468, 3828
- Väisänen P., Barway S., Randriamanakoto Z., 2014, *ApJL*, 797
- VandenBerg D.A., Brogaard K., Leaman R., Casagrande L., 2013, *ApJ*, 775, 134
- Worthey G., Ottaviani D. L., 1997, *ApJS*, 111, 377
- Worthey G., 1994, *ApJS*, 95, 107
- Worthey G., Faber S. M., Gonzalez J.J., Burstein D., 1994, *ApJS*, 94, 687
- Yong D., et al. 2014, *MNRAS*, 441, 3396 (Y14)

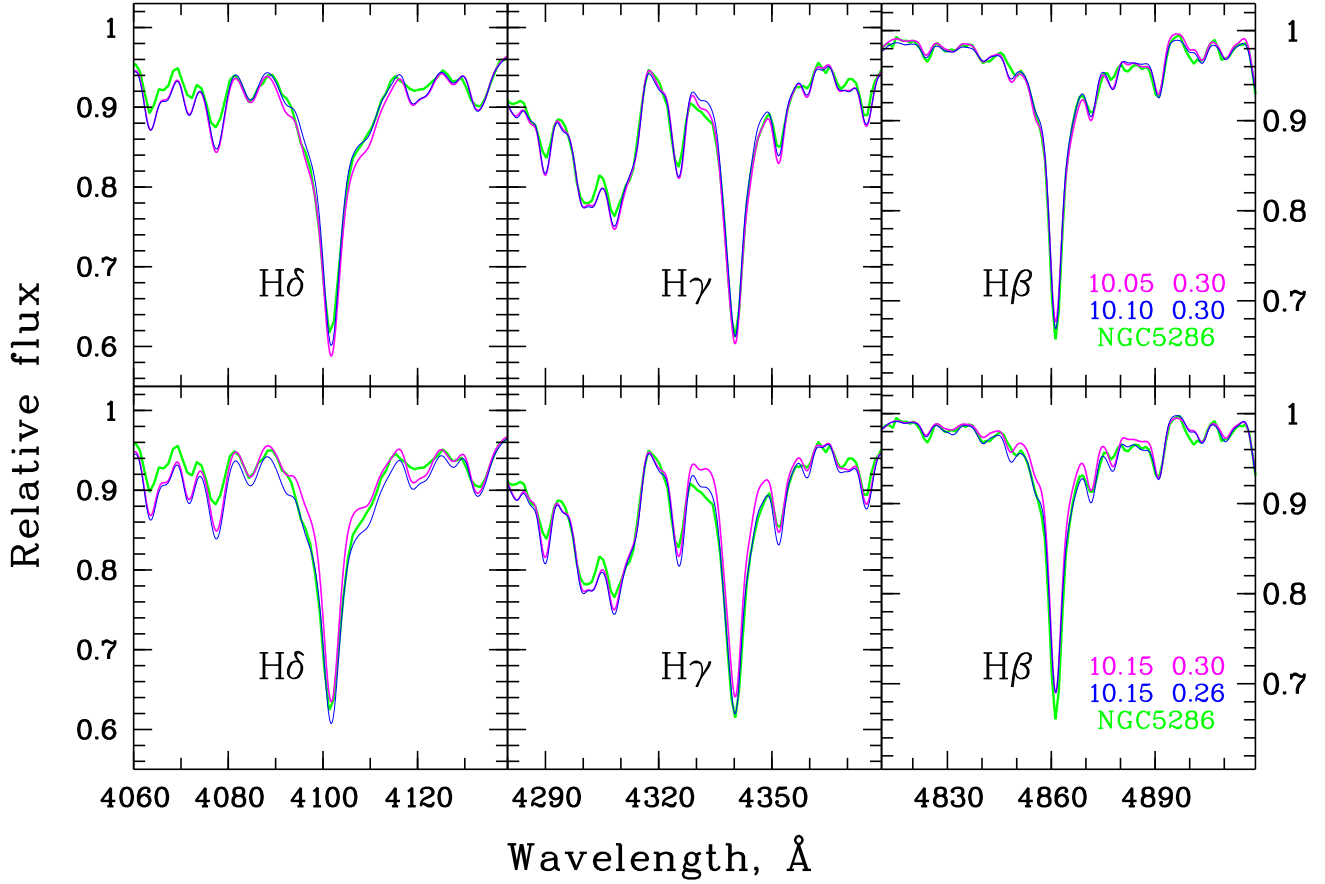


Figure A1. Comparison of the spectrum of NGC 5286 and computed synthetic integrated-light spectra of GCs in the ranges of the three Balmer lines. We used for the calculation the same elemental abundances valid for NGC 5286 (Table 4) and isochrones by Bertelli et al. 2008 of the same metallicity $Z = 0.0004$ and different age and specific helium abundance: $\log(\text{Age}) = 10.15$, $Y = 0.30$, $\log(\text{Age}) = 10.15$, $Y = 0.26$, $\log(\text{Age}) = 10.05$, $Y = 0.30$ and $\log(\text{Age}) = 10.10$, $Y = 0.30$.

APPENDIX A: DETERMINATION OF AGES AND HELIUM ABUNDANCES USING INTEGRATED SPECTRA OF GCS

Figures of this section illustrate our method of determination of ages and mean helium abundance (Y) using integrated spectra of GCs (Section 3.1 and references therein). Figure A1 compares the spectrum of NGC 5286 (green line) from Schiavon et al. (2005) with the synthetic spectra computed using four different isochrones by Bertelli et al. (2008). It can be seen that no isochrone describes exhaustively all the Balmer lines. The most suitable isochrone for fitting the spectrum of NGC 5286 is: $Z = 0.0004$, $\log(\text{Age}) = 10.10$, $Y = 0.30$. Fitting the spectrum of NGC 5286 with this isochrone is shown in Fig. 2 (Section 3.1). Figure A2 illustrates the comparison of the Balmer lines in the spectra of NGC 5286, 1904, 6254, 6752, and 7089. It can be seen that there is no exact coincidence between the Balmer lines in five spectra. The aforementioned dissimilarities can be attributed to the complexities of the HBs, differences in the signal-to-noise ratios in the spectra, Galactic field contamination and effects of stochastic fluctuations in a number of stars within the spectrograph field-of-view

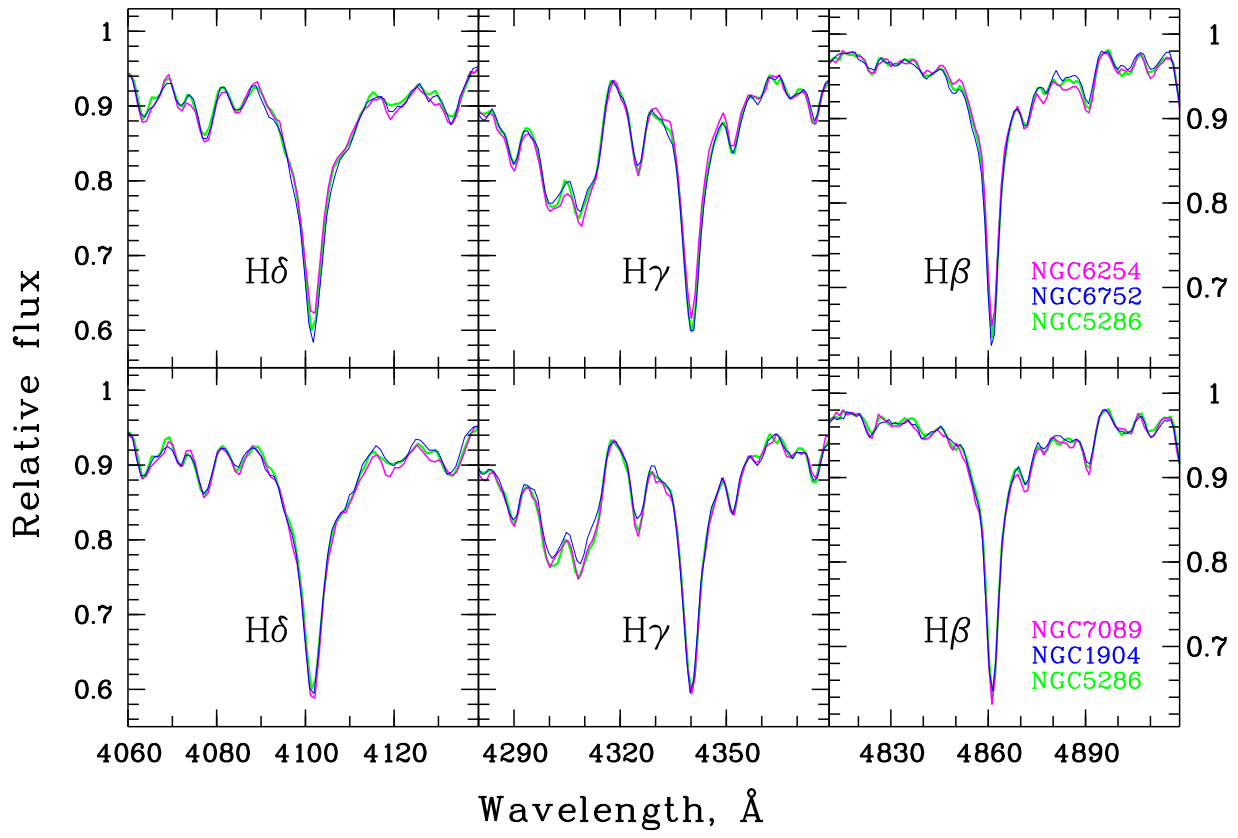


Figure A2. Comparison of the three Balmer lines in the spectra of NGC 5286, 1904, 6254, 6752 and 7089 .

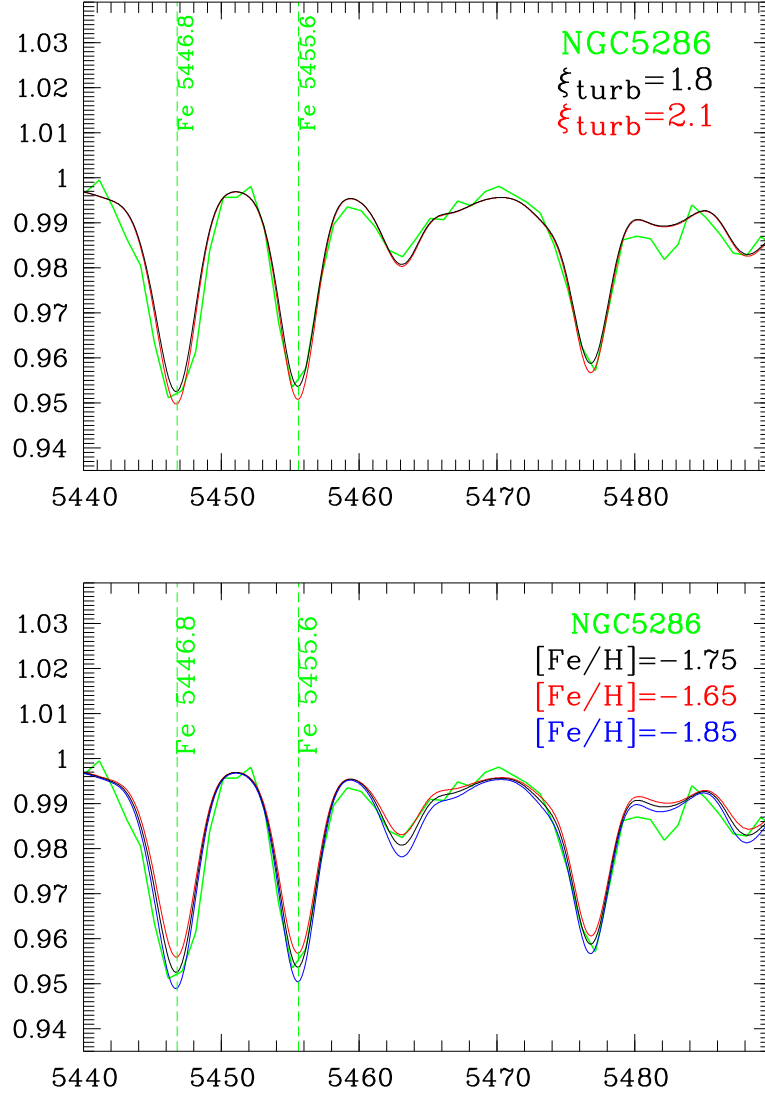


Figure B1. Spectrum of NGC 5286 (green line) in comparison to the synthetic spectra computed with different ξ_{turb} parameters (top) and different Fe abundances (bottom) and fixed other parameters. Relative flux is shown along the vertical axis. Wavelengths are along the horizontal axis.

APPENDIX B: DETERMINATION OF MICROTURBULENT VELOCITY AND FITTING THE ABUNDANCES OF DIFFERENT CHEMICAL ELEMENTS

This section illustrates the process of determination of Fe, Mg, Ca, C, and Cr abundances using medium-resolution integrated spectra of GCs. We use the spectrum of NGC 5286 (Schiavon et al. 2005) as an example. The method of chemical abundances determination is described in Section 3.1. The results are shown in Table 4 and described in Section 3.2. Figs B1 and B2 illustrate the influence of micro-turbulent velocity ξ_{turb} on the depths of Fe and Mg line blends in the synthetic spectra of GCs.

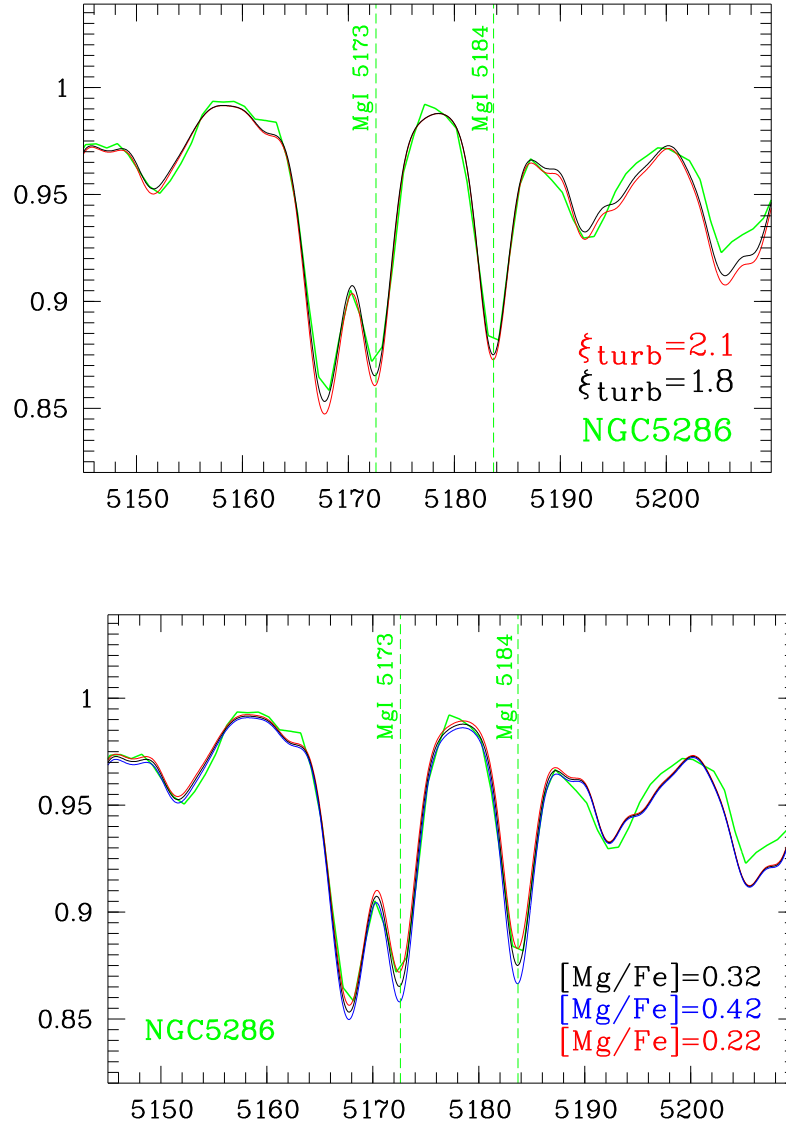


Figure B2. The same as in Fig. B1, but for Mg abundances.

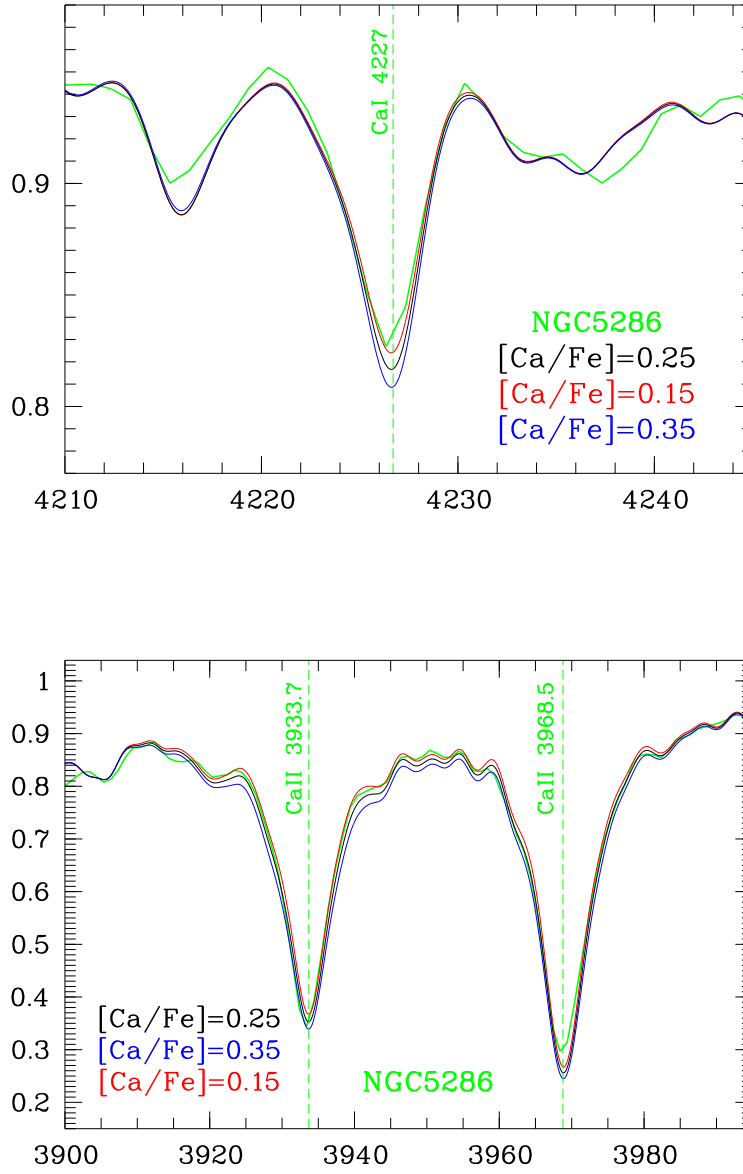


Figure B3. Spectrum of NGC 5286 (green line) in comparison to the synthetic spectra computed with different Ca abundance and fixed other parameters. Relative flux is shown along the vertical axis. Wavelengths are along the horizontal axis.

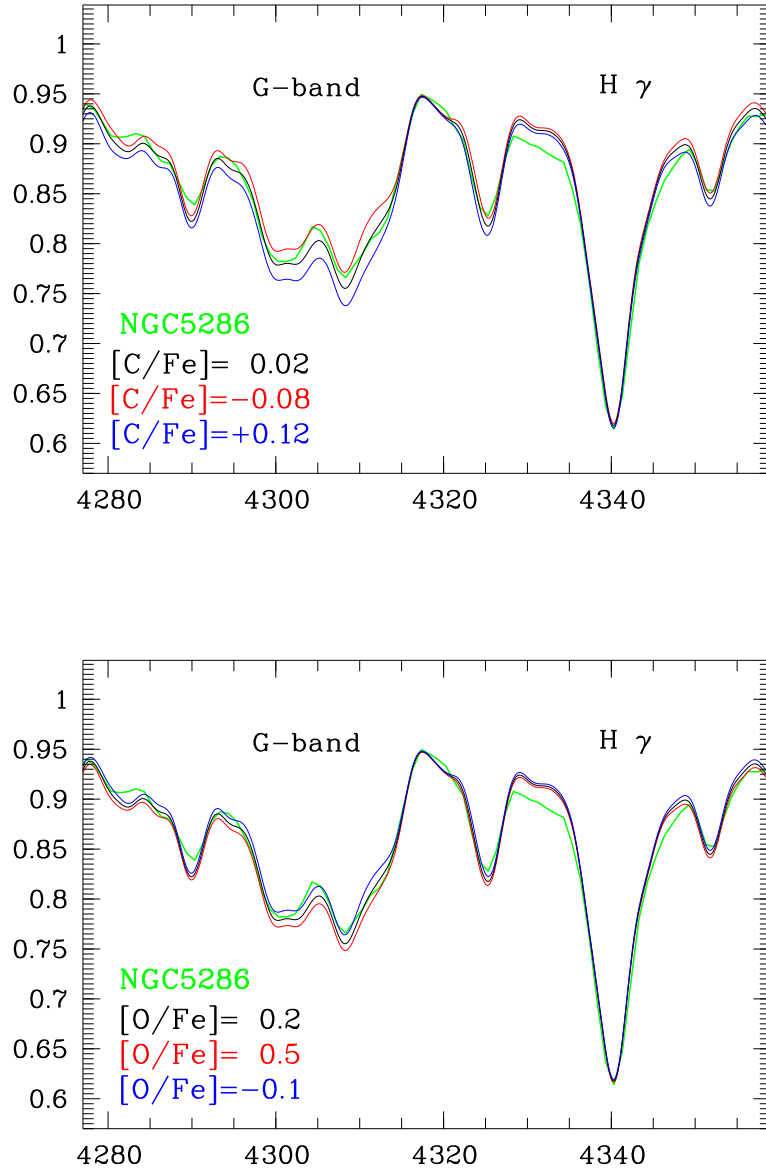


Figure B4. The same as in Fig. B3, but for C and O abundances.

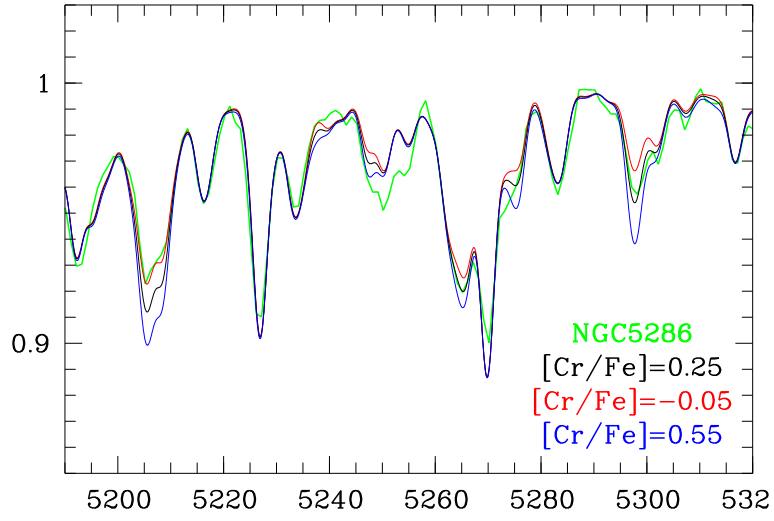


Figure B5. The same as in Fig. B3, but for Cr abundance.

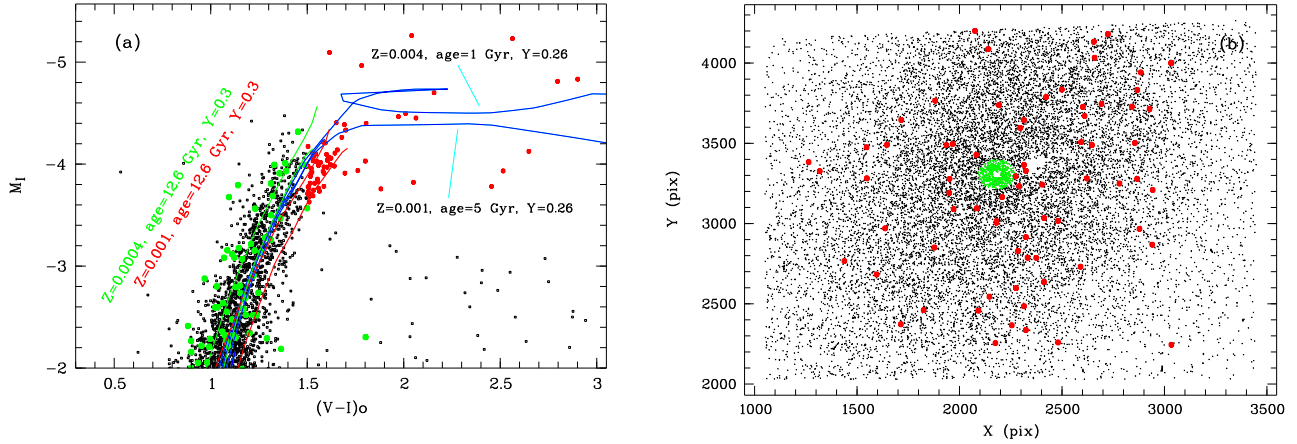


Figure C1. (a) CMD for a central region ($\sim 1 \times 1$ kpc) of KKS3. Stars within the radius of 47 pc around the centre of the GCs are shown in green. Bright red stars are shown as large red dots. Four isochrones (Bertelli et al. 2009) are overplotted. (b) Location of the stars shown in the panel (a) within the HST frame.

APPENDIX C: COMPARISON OF STELLAR PHOTOMETRIC DATA FOR KKS 3, ESO 269-66, AND FOR THEIR NUCLEI

High-quality photometric results for KKS3 were kindly provided by L.N. Makarova. Please, see the paper by Karachentsev et al. (2015b) for description of the data. Transformation of the stellar magnitudes from the instrumental F606W and F814W filters into the V and I bands of the Johnson-Cousins system was performed using the DOLPHOT package (Dolphin 2002). Objects with large photometric errors, or non-stellar shapes were eliminated from the analysis. Figure C1a shows a bright part of the galactic CMD for stars within the rectangular area of $\sim 2000 \div 2000$ pixels around the centre of the GC, which is equal to the projected area of $\sim 1 \times 1$ kpc. We used the distance modulus and extinction determined by Karachentsev et al. (2015b) (Table 1 in this paper). Green dots represent stars within a radius of ~ 47 pc ($4.6''$) from the centre of the GC. This is the area, where the azimuthally averaged surface brightness of the GC confidently exceeds the sky level around the cluster (Fig. 7). Four isochrones by Bertelli et al. (2008) are overplotted: $\log(\text{Age}) = 10.10$, $Y = 0.30$, $Z = 0.0004$ (green), $\log(\text{Age}) = 10.10$, $Y = 0.30$, $Z = 0.001$ (red), and two additional isochrones of higher metallicity and younger age. Only the bright parts of the RGB and AGB sequences are shown. Fig. C1b illustrates X and Y HST frame positions of the stars analysed in Fig. C1a. The central $1.6'' \times 1.8''$ region of the GC is empty of stars due to strong crowding effects. Another large empty region is located ~ 150 pixels to the right from the GC in KKS3. This is the place of a bright foreground star projection.

Similar analysis for stars in ESO 269-66 is demonstrated in Fig. C2. The magnitude, colour, and area selection criteria are the same as for KKS3. We use stellar photometry data from Sharina et al. (2008) obtained using the DOLPHOT package (Dolphin 2002). ESO 269-66 is brighter than KKS3 and almost twice more distant. There are much more RGB and AGB stars in ESO 269-66 than in KKS3 (Fig. C2a). Photometry of only 54 stars was possible within a radius of ~ 47 pc ($2.5''$) from the centre of the GC in ESO 269-66 (green dots in Fig. C2) due to strong crowding effects in the dense central $2.8'' \times 3.0''$ region of the GC. Average photometric uncertainties at the level of TRGB $I = 24.04$, $V - I \sim 1.6$ are: $\sigma_I \sim 0.1$ mag, $\sigma_V \sim 0.15$ mag (Karachentsev et al. 2007).

Figs C1a and C2a demonstrate that the stars within the boundaries of the GCs in both dSphs have a bluer colour on average (lower metallicity) than the rest of the upper RGB stars in the galaxies. Dispersion of stellar colours (metallicities) at $M_I = -3.5 \pm 0.1$ mag in KKS3 is lower [$\sigma(V - I) = 0.08$] than that in ESO 269-66 [$\sigma(V - I) = 0.19$] (Sharina et al. 2008).

Figs C1 and C2 show that stellar photometric data for the regions within a radius of ~ 47 pc around the centres of the GCs in KKS3 and ESO 269-66 do not contain bright red stars (red dots) with magnitudes and colours in the range: $M_I \leq -3.6$ mag and $(V - I)_0 \geq 1.56$ mag. Probable contribution of bright intermediate-age metal-rich stars in the central crowded regions of the clusters is 1–2 and 3–6 objects for KKS3 and ESO 269-66, respectively.

Our spectroscopic analysis and the data presented in this section indicate that intermediate-age and high-metallicity stellar populations do not contaminate significantly the integrated light of the studied GCs.

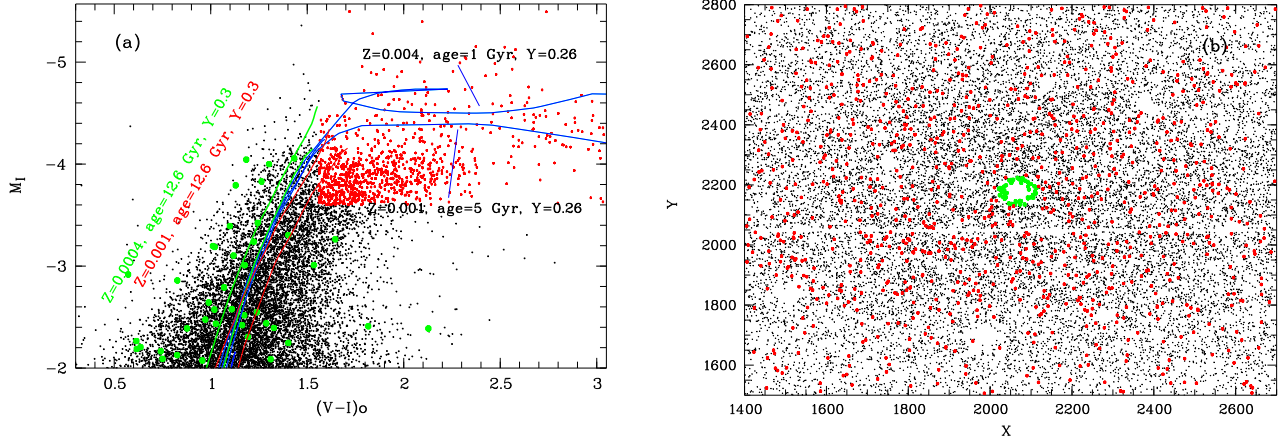


Figure C2. The same as in Fig. C1, but for ESO 269-66.

Table D1. Lick indices ($\lambda \leq 4531\text{\AA}$) (first line) measured in the spectra of nuclear GCs in KKS 3 and ESO 269-66 with the corresponding uncertainties (second line indicated by the "±" sign).

ID		H δ_A (\AA)	H γ_A (\AA)	H δ_F (\AA)	H γ_F (\AA)	CN ₁ (mag)	CN ₂ (mag)	Ca4227 (\AA)	G4300 (\AA)	Fe4383 (\AA)	Ca4455 (\AA)
GC in KKS 3		2.38	0.33	1.60	1.49	-0.080	-0.064	0.06	2.64	0.35	0.14
	±	0.10	0.12	0.12	0.12	0.006	0.006	0.05	0.11	0.12	0.08
GC in E269-66		2.94	0.63	1.99	1.53	-0.062	-0.060	0.09	2.01	0.23	0.31
	±	0.08	0.09	0.09	0.08	0.006	0.005	0.04	0.12	0.07	0.06

Table D2. Lick indices ($\lambda \geq 4531\text{\AA}$) (first line) measured in the spectra of nuclear GCs in KKS 3 and ESO 269-66 with the corresponding uncertainties (second line indicated by the "±" sign).

ID		Fe4531 (\AA)	Fe4668 (\AA)	H β (\AA)	Fe5015 (\AA)	Mg ₁ (mag)	Mg ₂ (mag)	Mgb (\AA)	Fe5270 (\AA)	Fe5335 (\AA)	Fe5406 (\AA)
GC in KKS 3		0.99	0.25	2.42	1.43	0.037	0.067	1.03	0.78	1.46	0.50
	±	0.09	0.17	0.06	0.15	0.003	0.003	0.04	0.06	0.08	0.05
GC in E269-66		1.78	0.41	2.34	1.30	0.021	0.075	0.78	0.94	1.04	0.73
	±	0.07	0.15	0.05	0.09	0.003	0.003	0.05	0.11	0.07	0.04

APPENDIX D: MEASURING OF LICK INDICES IN THE SPECTRA OF GCS IN KKS 3 AND E269-66

Absorption-line indices in the so-called Lick system (Burstein et al. 1984, Worthey et al. 1994, Worthey 1994, Worthey & Ottaviani 1997, Trager et al. 1998) offer a useful tool for disentangling age and metallicity effects on medium-resolution spectra of GCs and galaxies. In this section, we present the Lick indices for GCs in KKS3 and E269-66 measured using the flux-calibrated medium-resolution spectra (Section 2), the procedure described by Sharina et al. (2008), and the calibrations into the Lick standard system by Katkov, Kniazev & Sil'chenko (2015). Tables D1 and D2 present the indices and their measurement errors. Total errors of the Lick indices include the index measurement errors and the errors of transformation into the Lick standard system (including random and systematic effects). If the signal-to-noise ratio in the studied spectra is $S/N \geq 100$, the typical measurement errors are smaller than the errors of transformation into the Lick standard system (e.g. Schiavon et al. 2012). In the following we list typical total errors at $S/N \sim 100$ for the indices presented in Fig. D1: $\sigma(H\delta_A) \sim 0.7\text{\AA}$, $\sigma(H\beta) \sim 0.2\text{\AA}$, $\sigma(< Fe > = (Fe5270 + Fe5335)/2) \sim 0.25\text{\AA}$, $\sigma([Mg/Fe]' = \sqrt{Mgb(0.72Fe5270 + 0.28Fe5335)}) \sim 0.25\text{\AA}$, $\sigma Mgb \sim 0.15\text{\AA}$, $\sigma CN1 \sim 0.025$ mag, $\sigma Ca4227 \sim 0.2\text{\AA}$, and $\sigma G4300 \sim 0.35\text{\AA}$. These errors do not include the errors of simple stellar population models which are large at low metallicities (Thomas et al. 2011).

In Fig. D1 we compare the indices for GCs in KKS3 and E269-66 and the corresponding indices for several Galactic GCs of similar metallicity from Schiavon et al. (2012) and Schiavon et al. (2005). Galactic GCs in two metallicity groups are shown: 1) $[Fe/H] \sim -1.6$ dex (NGC 1904, 3201, 5986, 6254, 6333, 6752, and 7089) and 2) $[Fe/H] \sim -1.3$ dex (NGC 5904, 5946, 6218, and 6235). The α -enhanced simple stellar population (SSP) models by Thomas et al. (2003, 2004) are over-plotted. The upper two plots ($H\delta_A$ vs. $[Mg/Fe]'$ and $H\beta$ vs. $[Mg/Fe]'$) serve to disentangle the effects of age and metallicity on integrated spectra of GCs. Two groups of Galactic GCs with $[Fe/H] \sim -1.6$ dex and $[Fe/H] \sim -1.3$ dex are separated well and it is seen that the $[Mg/Fe]'$ data for the GCs in dSphs are approximately in between the two groups of Galactic GCs. The GC in KKS3 is slightly more metal-rich, and/or Mg-rich than the GC in ESO 269-66. The differences in the Balmer line indices are mainly caused by age and a number of hot HB stars contributing to the integrated spectra (e.g. Schiavon et al. 2004). It is surprising for us that the hydrogen line indices $H\delta_A$ and $H\beta$ are also almost identical for seven of nine Galactic GCs despite of their different HB morphologies (Harris, 1996). The influence of light elements on the spectra and the measured indices are seen in the lower four panels of Fig. D1. It is seen that the light-element content of the GCs in dSphs is close to that of the lower-metallicity group of Galactic GCs. CN1, Ca4227, and Mgb indices are almost identical for seven Galactic GCs with $[Fe/H] \sim -1.6$ dex. GC in KKS3 has roughly the same Ca and C abundance as the GC in ESO 269-66 and more abundant in nitrogen. All these qualitative conclusions agree with the results of our full spectrum fitting analysis using stellar atmosphere models (Sections 3.1 and 3.2).

This paper has been typeset from a \LaTeX file prepared by the author.

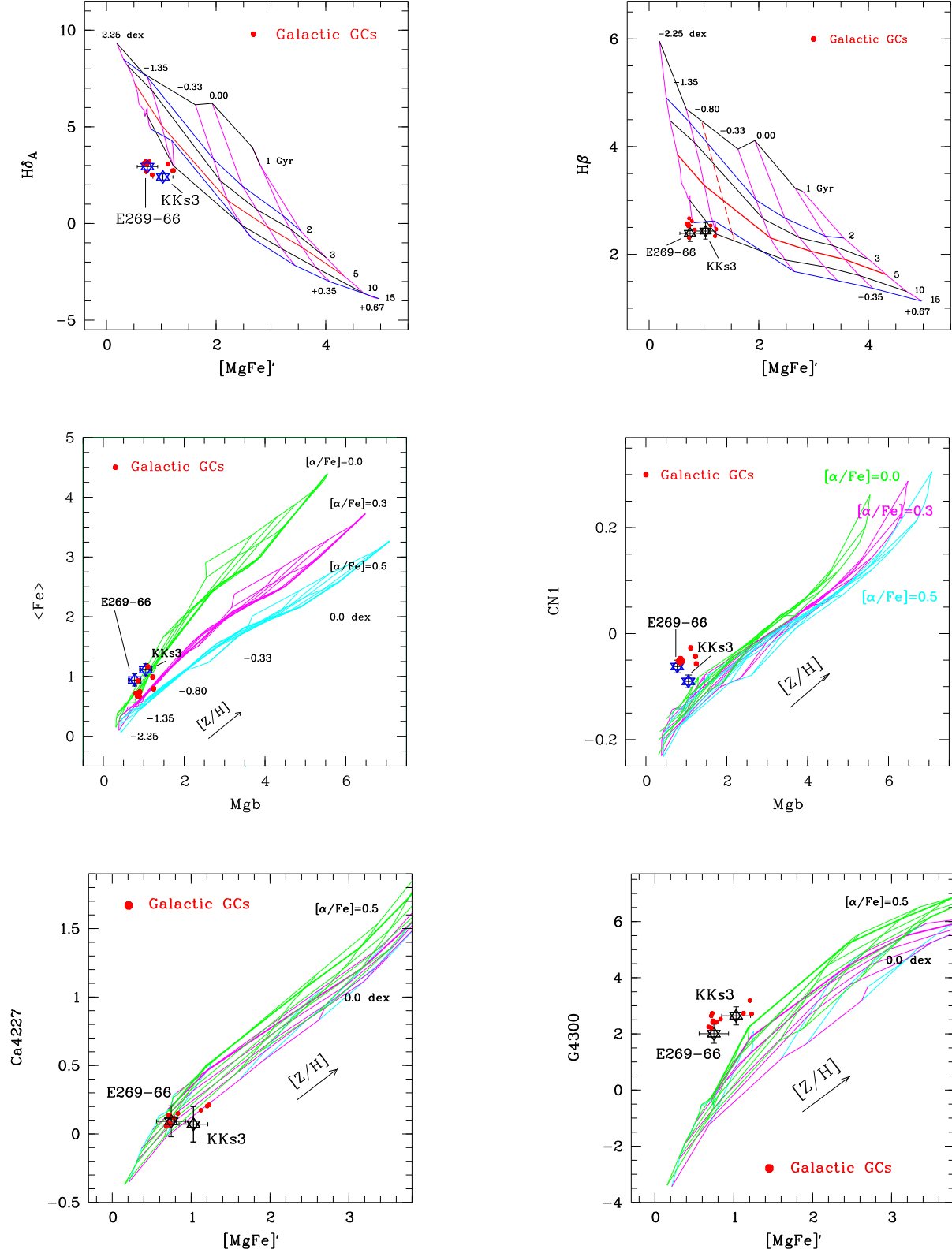


Figure D1. Lick-index diagnostic plots for GCs in Kks3 and E269-66 and for Galactic GCs (Schiavon et al. 2012) in two metallicity groups: 1) $[\text{Fe}/\text{H}] \sim -1.6$ dex (NGC 1904, 3201, 5286, 5946, 5986, 6254, 6333, 6752, 7089) and 2) $[\text{Fe}/\text{H}] \sim -1.3$ dex (NGC 5904, 5946, 6218, 6235). SSP models by Thomas et al. (2003, 2004) are overplotted.